DRP1-mediated mitochondrial fission is essential to maintain cristae morphology and bioenergetics

Gabriella L. Robertson[1], Stellan Riffle[1], Mira Patel[1], Andrea Marshall[2], Heather Beasley[2], Edgar Garza Lopez[2], Jianqiang Shao[3], Zer Vue[2], Antentor Hinton Jr.[2], Jason Mears[4], and Vivian Gama[1,5,6,7]

[1]Vanderbilt University, Cell and Developmental Biology, Nashville, TN.
[2]Vanderbilt University, Molecular Physiology and Biophysics, Nashville, TN.
[3]Central Microscopy Research Facility, University of Iowa, Iowa City, IA.
[4]Case Western Reserve University, Department of Pharmacology, Cleveland, OH.
[5]Vanderbilt University, Vanderbilt Center for Stem Cell Biology, Nashville, TN
[6]Vanderbilt University, Vanderbilt Brain Institute, Nashville, TN

[7]Corresponding author

Correspondence should be addressed to:

Vivian Gama
PMB407935
465 21st Avenue South, 4150A
Vanderbilt University
Nashville, TN 37240-7935
Tel: (615) 875-9490
vivian.gama@vanderbilt.edu

Running title: DRP1 mutations associated with EMPF1

Keywords: fibroblasts, DRP1, mitochondria, peroxisomes, cristae, glycolysis, oxidative phosphorylation

Abstract

Mitochondria and peroxisomes are both dynamic signaling organelles that constantly undergo fission. While mitochondrial fission is known to coordinate cellular metabolism, proliferation, and apoptosis, the physiological relevance of peroxisome dynamics and the implications for cell fate are not fully understood. DRP1 (dynamin-related protein 1) is an essential GTPase that executes both mitochondrial and peroxisomal fission. Patients with *de novo* heterozygous missense mutations in the gene that encodes DRP1, *DNM1L*, present with encephalopathy due to defective mitochondrial and peroxisomal fission (EMPF1). EMPF1 is a devastating neurodevelopmental disease with no effective treatment. To interrogate the mechanisms by which DRP1 mutations cause cellular dysfunction, we utilized human-derived fibroblasts from patients with mutations in DRP1 who present with EMPF1. As expected, patient cells display elongated mitochondrial morphology and lack of fission. Patient cells display a lower coupling efficiency of the electron transport chain, increased proton leak, and upregulation of glycolysis. In addition to these metabolic abnormalities, mitochondrial hyperfusion results in aberrant cristae structure and hyperpolarized mitochondrial membrane potential, both of which are tightly linked to the changes in metabolism. Peroxisome structure is also severely elongated in patient cells and results in a potential functional compensation of fatty acid oxidation. Understanding the mechanism by which DRP1 mutations cause these metabolic changes will give insight into the role of mitochondrial dynamics in cristae maintenance and the metabolic capacity of the cell, as well as the disease mechanism underlying EMPF1.

53 **Introduction**

54 Mitochondrial dynamics are controlled and executed by a vast group of proteins and other
55 organelles. The underlying morphology of the mitochondria is an important determinant for the
56 ability of this organelle to regulate a variety of cellular processes, such as apoptosis, cell fate, lipid
57 biosynthesis, and epigenetic modifications (Bayraktar et al., 2019; Iwata et al., 2020; Khacho et
58 al., 2016; King et al., 2021; Prigione and Adjaye, 2011; Rasmussen et al., 2020; Vantaggiato et
59 al., 2019). Mitochondrial fusion is primarily catalyzed by the large GTPases Mitofusin 1 and
60 Mitofusin 2 at the outer mitochondrial membrane (Chen et al., 2003). The GTPase OPA1 is
61 responsible for executing fusion of the inner mitochondrial membrane (Alexander et al., 2000;
62 Delettre et al., 2000). Mitochondrial fission, mediated through the large GTPase DRP1 (Dynamin-
63 related protein 1), is orchestrated by a complex sequence of events (Fonseca et al., 2019;
64 Smirnova et al., 2001). The first steps of mitochondrial fission include contact with the
65 endoplasmic reticulum (ER) and replication of the mitochondrial genome (Friedman et al., 2011;
66 Lewis et al., 2016). This is followed by contact and pre-constriction by actin filaments, which are
67 associated with the ER membrane (Chakrabarti et al., 2018; Hatch et al., 2016, 2014; Ji et al.,
68 2017, 2015; Li et al., 2015). Fission is also regulated through adaptor proteins at the outer
69 mitochondrial membrane, including MiD49, MiD51, MFF, and FIS1, however, their distinct roles
70 in fission are not completely understood (Losó n et al., 2013; Osellame et al., 2016; Palmer et al.,
71 2013). After the association with adaptor proteins, DRP1 then forms a 12-dimer ring around the
72 mitochondria and hydrolyzes GTP to GDP causing a confirmational change in the ring that
73 executes fission (Chang and Blackstone, 2007; Fröhlich et al., 2013; Nagashima et al., 2020).
74 DRP1 is essential for mitochondrial fission and without functional DRP1, the mitochondrial
75 network becomes hyperfused. In addition to the effects on mitochondrial morphology, DRP1 also
76 mediates the fission of peroxisomes (Koch et al., 2003). Peroxisomes are highly specialized
77 organelles vital for the beta oxidation of very-long-chain fatty acids, detoxification of reactive

78 oxygen species (ROS), production of cholesterol, bile acids, and plasmalogens, which contribute
79 to the phospholipid content in the brain white matter (Chandel, 2021; Ding et al., 2021; Ferreira
80 et al., 2021; Lodhi and Semenkovich, 2014; Ravi et al., 2021; Schrader et al., 2020; Sugiura et
81 al., 2017). The adaptor proteins MFF and FIS1 are also involved in DRP1 recruitment to sites of
82 peroxisome fission (Gandre-Babbe and Van Der Bliek, 2008; Itoyama et al., 2013; Koch and
83 Brocard, 2012). The contacts between mitochondria and peroxisomes are essential for linking
84 peroxisomal β-oxidation and mitochondrial ATP generation by the ETC, maintenance of redox
85 homeostasis, and lipid transfer (Chandel, 2021; Fan et al., 2016; Fransen et al., 2017). Thus,
86 peroxisomal and mitochondrial metabolic activities are functionally interconnected. Consistent
87 with this, peroxisomal disorders caused by mutations in genes involved in the biogenesis and
88 function of peroxisomes, are often associated with mitochondrial dysfunction (Tanaka et al.,
89 2019). This communication may be particularly important during brain development and metabolic
90 stress. However, the molecular mechanisms that facilitate this communication are still poorly
91 understood.

92 In mouse models, global DRP1 knockout is embryonic lethal (Ishihara et al., 2009; Wakabayashi
93 et al., 2009). With the advent of exome sequencing, patients with *de novo* mutations in the gene
94 that encodes DRP1, *DNM1L (Dynamin 1 Like)*, have been identified (Chao et al., 2016; Fahrner
95 et al., 2016; Keller et al., 2021; Liu et al., 2021; Longo et al., 2020; Nasca et al., 2016; Nolan et
96 al., 2019; Ryan et al., 2018; Sheffer et al., 2016; Vandeleur et al., 2019; Waterham et al., 2007).
97 The disease associated with mutations in *DNM1L* is known as encephalopathy due to defective
98 mitochondrial and peroxisomal fission-1 (EMPF1). Most reported mutations are heterozygous
99 missense mutations. Patients present with heterogeneous symptoms including
100 neurodevelopmental delay, seizures, muscle abnormalities, and ataxia. Patient fibroblasts show
101 very elongated mitochondrial networks and elevated lactate levels, suggesting an impairment in
102 oxidative phosphorylation (Liu et al., 2021; Whitley et al., 2018). Currently, there is no effective

103 treatment or cure for patients effected by DRP1 mutations. The life expectancy for most patients
104 with DRP1 mutations is childhood to early adolescence (Ryan et al., 2018). Although other
105 proteins and organelles are involved in fission, DRP1 has been shown to be indispensable for
106 mitochondrial fission (Csordás et al., 2006; Fonseca et al., 2019; Kamerkar et al., 2018; Li et al.,
107 2015; Nagashima et al., 2020; Smirnova et al., 2001), yet the cellular consequences of DRP1
108 dysfunction are not well understood. In this study, we aimed to characterize the effects of two
109 mutations in DRP1 identified in patients with EMPF1, the G32A mutation, which lies in the catalytic
110 GTPase domain of DRP1, and the R403C mutation, which lies in the stalk domain (Fröhlich et al.,
111 2013), on mitochondrial network morphology, cristae ultrastructure, and related metabolic
112 adaptations, to gain fundamental insight into the cellular adaptations to dysfunctional organelle
113 fission and the pathophysiology of EMPF1.

114 Here, we resolve and quantify mitochondrial and peroxisomal morphological features associated
115 with EMPF1-associated mutations and reveal their impact on cellular metabolism, to put into
116 perspective the clinical findings that were previously described (Fahrner et al., 2016; Liu et al.,
117 2021; Ryan et al., 2018). We found that the inability of DRP1 to fragment the mitochondria in
118 patient-derived fibroblasts leads not only to the hyperfusion phenotype previously described, but
119 also to delayed cell death in response to apoptotic signals, aberrant mitochondrial cristae
120 structure, and hyperpolarized mitochondrial membrane potential. Metabolically, the changes in
121 mitochondrial and peroxisomal morphology result in inefficiency of the electron transport chain
122 coupling oxygen consumption with ATP production and upregulation of glycolysis. Altogether,
123 these data indicate that mitochondrial and peroxisomal fission influence dynamics of the inner
124 mitochondrial membrane and the metabolic state of the cell.

125

126 **Results**

127 **DRP1 variants found in patients have dominant negative effects that alter the expression**
128 **of critical proteins at the mitochondria**

129 Light microscopy studies have shown the profound alterations of mitochondrial fission in cells
130 from patients harboring mutations in DRP1 (Ryan et al., 2018; Whitley et al., 2018). These studies
131 highlighted the clinical relevance of mitochondrial fission in neural development. We quantified
132 the morphology of the mitochondria in patient-derived primary fibroblasts at super resolution level
133 using structured illumination microscopy (SIM). Both patient fibroblast lines showed increased
134 mitochondrial volume, surface area and major axis length, consistent with a hyperfused
135 mitochondrial morphology, as reported for DRP1 null cells (Fonseca et al., 2019; Kamerkar et al.,
136 2018; Smirnova et al., 2001) (Fig. 1A-B). Live-cell imaging of mitochondria stained with
137 MitoTracker confirmed that mitochondrial fission events are rare in patient cells compared to
138 control fibroblasts (Supplementary Fig. 1A). High resolution three-dimensional images of control
139 and patient fibroblasts were obtained using serial block facing-scanning electron microscopy
140 (SBF-SEM) (Garza-Lopez et al., 2021). Manual segmentation and stack reconstruction of the
141 mitochondrial networks validated the increased length and volume of the mitochondrial networks
142 as well as increased mitochondrial complexity index (MCI) in patient fibroblasts (Fig. 1C-D). MCI
143 is a quantitative measurement of network complexity, which takes into account both volume and
144 surface area of the mitochondria (MCI = $SA^3 / 16\pi^2V^2$) (Faitg et al., 2021; Vincent et al., 2019).
145 Both mutations in DRP1 result in significant alterations of the mitochondrial network with G32A
146 fibroblasts showing slightly more severe elongation than R403C (Fig. 1D and Supplementary Fig.
147 1B).

148 Both mutations in DRP1 are found to be heterozygous in patients, suggesting that mutant DRP1
149 has a dominant effect that can interfere with the ability of wild-type DRP1 to fragment the
150 mitochondria. Previous studies have demonstrated that the GFP can interfere with the activity of

151 DRP1 (Montecinos-Franjola et al., 2020). Thus, we generated mCherry tagged- constructs
152 containing the patient derived mutations and expressed them in human fibroblasts homozygous
153 for endogenous wild-type DRP1. Overexpression of mCherry-DRP1-G32A and mCherry-DRP1-
154 R403C by transient transfection in wild-type fibroblasts demonstrated that, as previously
155 described (Fahrner et al., 2016; Ryan et al., 2018; Whitley et al., 2018), the mitochondrial
156 hyperfusion seen in patient cells is not due to the genetic background and that these mutations
157 act in a dominant negative manner (Fig. 1E-F). While both mutations of DRP1 significantly
158 impaired DRP1 function in human fibroblasts, the G32A show a slightly more severe phenotype
159 than R403C.

160 Hyperfusion of the mitochondrial membrane due to sequestration and inactivation of DRP1 is
161 thought to lead to unopposed fusion events that increase the severity of mitochondrial elongation
162 (Palmer et al., 2013). We examined the effects of DRP1 mutations on the protein expression
163 levels of mitochondrial dynamics proteins. Both Mitofusin 1 and Mitofusin 2 were expressed at
164 lower levels in patient cells than in control cells. However, there was no significant difference in
165 the expression of OPA1 (Fig. 2A). These data show that there is a reduction in the expression of
166 mitochondrial outer membrane fusion proteins in patient cells, suggesting that active
167 mitochondrial fission promotes protein stability at the outer mitochondrial membrane. These data
168 also indicate that aberrant fission caused by DRP1 mutations may not alter fusion dynamics at
169 the inner mitochondrial membrane.

170 Phosphorylation of DRP1 at Serine 616 has been proposed to be a critical determinant of DRP1
171 recruitment and activity (Koch and Brocard, 2012; Taguchi et al., 2007; Valera-Alberni et al.,
172 2021). Whether mutations in DRP1 found in patients with EMPF1 affect the levels of
173 phosphorylation at Serine 616 has not been explored. We examined DRP1 levels in patient
174 derived fibroblasts. Although there was no significant difference in total DRP1 expression, G32A
175 patient cells expressed significantly less pS616-DRP1 (Fig. 2B). Since G32A mutation impairs

176 DRP1 phosphorylation to a greater extent than the R403C mutation, the GTPase domain of DRP1
177 may be structurally or functionally involved in interactions with kinases responsible for DRP1
178 phosphorylation. We wondered whether the expression of one copy of mutant DRP1 in patient
179 fibroblasts affected the recruitment of endogenous pS616-DRP1 to the mitochondria. To test this,
180 we quantified the recruitment of phosphorylated DRP1 to the outer mitochondrial membrane using
181 super-resolution microscopy. On average, there was no significant difference in the recruitment
182 of pS616-DRP1 to the mitochondria in patient cells and control cells (Fig. 2C-D). While in all cell
183 lines, pS616-DRP1 was found in close contact to the mitochondrial membrane, in the patient
184 fibroblasts this interaction appeared less transient. These results point to generalized stalling of
185 the fission events in patient fibroblasts.

186 The onset of apoptosis is accompanied by mitochondrial remodeling, stable association of DRP1
187 to the mitochondrial membrane, and increased fragmentation of the mitochondrial membrane
188 (Martinou and Youle, 2006; Wasiak et al., 2007). In DRP1 deficient cells, this remodeling of
189 mitochondria is significantly reduced and the onset of cell death is delayed (Lee et al., 2004). To
190 determine the effects of mitochondrial stress on mitochondrial fragmentation in patient fibroblasts,
191 we quantified changes in mitochondrial fission in response to CCCP treatment. As previously
192 shown using RNAi experiments in HeLa cells, patient fibroblasts showed reduced mitochondrial
193 fragmentation induced by CCCP compared to control cells (Fig. 2E-F). Although some
194 mitochondrial fragmentation may occur, mitochondrial volume and major axis length are
195 significantly larger in patient cells treated with CCCP than control cells. Upon apoptosis, BAX
196 translocates to the mitochondria and cytochrome c is released to the cytosol (Smaili et al., 2001).
197 While in DRP1 depleted cells BAX is recruited to the mitochondria, cytochrome c release is
198 delayed. Consistent with this, patient fibroblasts show higher cell survival when treated with CCCP
199 and Etoposide; as well as, lower caspase-3 activity than control fibroblasts when treated with STS
200 (Supplementary Fig. 2A-B). Interestingly, basal levels of both BAX and BAK are significantly

201 reduced in patient fibroblasts with mutations in DRP1 (Supplementary Fig. 2C). Levels of the anti-
202 apoptotic protein MCL-1 were significantly reduced in G32A fibroblasts but not in R403C
203 fibroblasts, while BCL-XL expression levels remained relatively constant in all cell lines. Thus,
204 patient fibroblasts may display a compensatory adaptation to reduce the basal levels of BAX/BAK
205 activation. Whether this reduction in the ability to undergo apoptosis in response to mitochondrial
206 stress is a widespread phenomenon in all tissues of EMPF1 patients and/or whether apoptosis
207 inhibition results in deleterious accumulation of mitochondrial and nuclear DNA encoded
208 mutations remains unexplored. No significant alteration in the protein expression of DRP1
209 adaptors was detected (Supplementary Fig. 2D)

210 **Mitochondrial hyperfusion in DRP1 mutant fibroblasts leads to higher glycolytic rate and**
211 **increased mitochondrial membrane potential**

212 Mitochondrial morphology is tightly linked to metabolic function (Dorn, 2015; Wai and Langer,
213 2016); thus, we assessed the effects of DRP1 patient mutations on cellular metabolism by
214 measuring rates of glycolysis and oxidative phosphorylation (OXPHOS) in cells using a Seahorse
215 XF Analyzer. The Seahorse analyzer measures extracellular oxygen consumption as a readout
216 of OXPHOS and extracellular acidification as a readout of glycolysis. Basal and maximal oxygen
217 consumption was not significantly different in mutant cells compared to control, suggesting no
218 major defects in ATP production (Fig. 3A). However, proton leak was significantly higher in the
219 G32A patient cells and coupling efficiency was significantly lower in both patient lines (Fig. 3B).
220 Therefore, although basal ATP production is not perturbed in the mutant cells, the electron
221 transport chain is not effectively coupling substrate oxidation and ATP synthesis. Extracellular
222 acidification rate was significantly increased in both patient lines, consistent with an upregulation
223 of glycolysis (Fig. 3A) and the hyperlactacidemia observed in more than 50% of patients with
224 mutations in DRP1 (Liu et al., 2021). A glycolytic rate assay confirmed that both basal and
225 compensatory glycolysis are higher in both patient lines (Fig. 3C). Thus, although the cells are

226 capable of producing ATP, DRP1 mutations cause a defect in OXPHOS efficiency and metabolic
227 dependency on glycolysis (Fig. 3D).

228 The upregulation of glycolysis with no accompanied increase in oxidative phosphorylation led us
229 to interrogate a potential impairment in pyruvate transport. Two proteins are essential for
230 mitochondrial pyruvate transport in humans, Mitochondrial Pyruvate Carrier 1 and 2 (MPC1 and
231 MPC2) (Bricker et al., 2012; Herzig et al., 2012). MPC1 and MPC2 associate to form an ~150-
232 kilodalton complex in the inner mitochondrial membrane. We examined the expression of MPC1
233 and MPC2, using Western blot, which revealed a significant decrease in MPC2 expression in the
234 R403C cells (Fig. 3E). Real time quantitative PCR (RT-qPCR) gene expression analysis showed
235 a significant downregulation of *MPC2* expression in R403C cells and *MPC1* in both patient lines
236 (Fig. 3F). Taken together these data suggest that the upregulation in glycolysis seen in DRP1
237 mutant patient fibroblasts is a compensatory mechanism for impaired pyruvate import into the
238 mitochondria and/or decreased coupling efficiency of the ETC.

239 The major contributor of the proton motive force of the ETC is the mitochondrial membrane
240 potential, which drives oxidative phosphorylation. Thus, changes in OXPHOS coupling efficiency
241 can point to perturbation of the mitochondrial membrane potential and the maintenance of key ion
242 gradients. We investigated this possibility using the fluorescent sensor Tetramethylrhodamine,
243 ethyl ester (TMRE). TMRE is a cell-permeant, cationic, red-orange fluorescent dye that is
244 sequestered by polarized mitochondria. We found that mitochondrial membrane potential as
245 reported by TMRE was significantly increased in patient fibroblasts (Fig. 4), indicative of
246 hyperpolarization of the mitochondria.

247 **DRP1 mutations alter mitochondrial cristae morphology**

248 Cristae topology readjustments participate in energy balance control (Eramo et al., 2020; Kondadi
249 et al., 2020). The hyperpolarization of the mitochondrial membrane detected in patient fibroblasts

250 lead us to assess the effects of DRP1 mutations on cristae morphology. We used a previously
251 optimized method to quantify and analyze cristae morphology changes from transmission electron
252 microscopy (TEM) (Eisner et al., 2017; Lam et al., 2021). In this method, cristae abundance is
253 calculated by manually quantifying the number of cristae per mitochondrion, and a score between
254 0 (worst) and 4 (best) is assigned based on the morphology: (0—no well-defined cristae, 1—no
255 cristae in more than ~75% of the mitochondrial area, 2—no cristae in approximately ~25% of
256 mitochondrial area, 3—many cristae (over 75% of area) but irregular, 4—many regular cristae)
257 (Supplementary. Fig 3A). TEM of patient fibroblasts confirmed the mitochondrial elongation
258 observed in SIM (Supplementary Fig. 3B-D) and revealed differences in the cristae structure (Fig.
259 5A). The quantification of cristae morphology demonstrated a reduced cristae score and
260 decreased cristae number relative to mitochondrial length in DRP1-deficient cells compared with
261 the control cells (Fig. 5B). These data link aberrant outer mitochondrial membrane fission caused
262 by DRP1 mutations to generalized cristae structural changes. The structure and respiratory
263 function of mitochondrial cristae are maintained by the mitochondrial contact sites and cristae
264 organizing system (MICOS) complex – a large complex of scaffolding and membrane shaping
265 proteins localized at the inner mitochondrial membrane. Given the reduced cristae score, we
266 examined expression of some key components of the MICOS complex. *MIC19, MIC25,* and
267 *MIC60* are all reduced in either one or both patient lines at the mRNA level; however, protein
268 expression is not significantly changed (Supplementary. Fig. 4). The data suggest that the
269 structural abnormalities seen in patient fibroblasts are not due to changes in the expression of
270 proteins of the MICOS complex. Additional biochemical assays are needed to assess the
271 functionality of these proteins in the context of EMPF1.

272 **Patient fibroblasts display hyperfused peroxisomes**

273 In addition to catalyzing mitochondrial fission, DRP1 also participates in peroxisomal fission
274 (Kamerkar et al., 2018). While fission of peroxisomes has been demonstrated to be involved in

275 *de novo* peroxisomal biogenesis, the functional consequences of peroxisomal fission are not
276 completely understood. Previous reports using EMPF1 patient fibroblasts have not reported
277 elongation of peroxisomes, but DRP1 null cells have been reported to have hyperfused
278 peroxisomes (Kamerkar et al., 2018). To interrogate the effects of DRP1 mutations on peroxisome
279 morphology, we performed super-resolution microscopy. SIM revealed that both mutations in
280 DRP1 result in significant elongation of peroxisomes (Fig. 6A). Quantification of the peroxisome
281 structure shows an increase in volume, surface area, and length of peroxisomes (Fig. 6B). These
282 data confirm that DRP1 mutations found in patients with EMPF1 result in impaired peroxisome
283 fission.

284 Since peroxisomes and mitochondria are hubs for the regulation of fatty acid metabolism, we first
285 tested whether the dramatic changes in morphology would alter the expression of key genes
286 involved in fatty acid oxidation in patient fibroblasts. The expression of these genes have
287 previously been reported to increase in a DRP1 phosphomimetic mouse model (Valera-Alberni et
288 al., 2021). RT-qPCR analysis showed that the expression of carnitine palmitoyltransferase I,
289 *CPT1*, and acyl-coA dehydrogenase medium chain, *ACADM*, are significantly lower in patient
290 cells compared to control (Fig. 6C). CPT1 is associated with the outer mitochondrial membrane
291 and is responsible for catalyzing the transfer of the acyl group of acyl-CoA to L-carnitine. Fatty
292 acids are then able to move from the cytosol into the inner membrane space of the mitochondria
293 and the matrix, where fatty acid oxidation occurs. *ACADM* encodes for the medium-chain-acyl-
294 CoA dehydrogenase (MCAD) protein, which catalyzes the first step of mitochondrial fatty acid
295 beta-oxidation. Thus, the reduction in *CPT1* and *ACADM* expression may hinder the ability of the
296 mitochondria to carryout fatty acid oxidation.

297 To examine the ability of patient fibroblasts to perform fatty acid oxidation, we used the Seahorse
298 analyzer to quantify oxygen consumption rates of patient fibroblasts treated with either vehicle or
299 etomoxir, a CPT1 inhibitor. The cells were cultured with minimal glucose and glutamine and high

300 L-carnitine and palmitate to promote fatty acid oxidation over glycolysis or glutaminolysis. Control
301 fibroblasts treated with etomoxir, an inhibitor of CPT1, show a reduction in maximal respiration
302 following FCCP injection. In contrast, the G32A patient-derived cells show no change in OCR with
303 etomoxir treatment and the R403C patient-derived cells show an increase in maximal respiration
304 following FCCP injection (Fig. 6D and Supplementary Fig. 5). These data indicate that in contrast
305 to the reliance of control cells to long chain fatty acid oxidation under conditions of maximal
306 respiration, both patient lines have lost this dependency and adapted to the inhibition of long-
307 chain fatty acid import into mitochondria under these conditions. These data show that fibroblasts
308 with DRP1 mutations appear to have compensatory adaptations to alterations in long-chain fatty
309 acid oxidation.

310

311 **Discussion**

312 DRP1 is an essential gene for embryonic development (Ishihara et al., 2009; Wakabayashi et al.,
313 2009). RNAi based approaches in human cell culture models have been used to explore the
314 impact of DRP1 loss on mitochondrial fission and downstream processes such as apoptosis and
315 mitophagy (Kleele et al., 2021; Otera et al., 2016; Smirnova et al., 2001). Although loss of DRP1
316 results in mitochondrial hyperfusion, it's not fully understood how mutations in DRP1 can impact
317 cellular metabolic function, cristae structure, and/or peroxisomal function. The analysis of
318 organelle morphology in fibroblast lines derived from patients with EMPF1 that harbor one wild-
319 type copy of DRP1 and one missense copy of DRP1, demonstrate a dominant negative effect of
320 mutant DRP1 that results in stalling of the fission machinery that has a wide impact on cellular
321 function.

322 Mitochondrial fission is essential for cellular processes such as apoptosis, mitophagy, and
323 mitochondrial biogenesis. However, how mitochondrial fission helps maintain cristae structure
324 and/or cellular metabolism have not been thoroughly explored. Our studies revealed that while in
325 EMPF1 patient lines, DRP1 is recruited to the mitochondria, the fission event is incomplete, and
326 thus, mitochondrial fission is paused. This stalling of mitochondrial fission results in dramatic
327 changes to cristae morphology, notably a decrease in cristae score and number, indicative of
328 immature and poorly formed cristae. Changes in redox signaling can lead to cysteine oxidation of
329 MIC60 (Li et al., 2021; Wasilewski and Chacinska, 2021), an inner mitochondrial membrane
330 protein responsible for cristae structure integrity. Thus, the lack of proper mitochondrial fission in
331 patient cells may disrupt redox signaling, which may in turn be responsible for the aberrant cristae
332 morphology detected in patient cells.

333 Detailed metabolic analysis of patient fibroblasts showed that these cells have decreased
334 coupling efficiency and upregulation of glycolysis, suggesting that the functional impact of stalled
335 fission is electron transport chain inefficiency. This inefficiency may be due to the changes in

336 cristae structure, since cristae structure is essential for F_0F_1–ATPase to function effectively (Afzal
337 et al., 2021; Cogliati et al., 2013; Davies et al., 2011; Wilkens et al., 2013). Previous studies
338 revealed that there are distinct fission signatures that are key determinants of the decision of
339 mitochondria to proliferate or degrade (Kleele et al., 2021). Peripheral fission events were shown
340 to be preceded by a decrease in membrane potential and proton motive force. We found that the
341 elongated mitochondria from patient fibroblasts have a hyperpolarized membrane potential, which
342 could result from inefficient function of the F_0F_1–ATPase. Under certain conditions, the F_0F_1–
343 ATPase can pump protons out of the mitochondrial matrix into the intermembrane space in a
344 reverse-mode action, causing ΔΨm hyperpolarization. Alternatively, hyperpolarization may be
345 due to complex I inhibition or VDAC (voltage-dependent anion channel) opening, which can cause
346 hyperpolarization independently of F_0F_1–ATPase reverse-mode action (Forkink et al., 2014). A
347 comprehensive analysis of the functionality of the ETC complexes would be needed to elucidate
348 the connection between fission stalling events and mitochondrial hyperpolarization. Upregulation
349 of glycolysis in these patient fibroblasts could result in subsequent glucose depletion locally within
350 the cells, which could in turn cause ΔΨm hyperpolarization. Carbon-tracing could help reveal
351 whether all of the products of glycolysis are efficiently shuttled into the TCA cycle or if
352 intermediates are lost in the process. Investigating the function of uncoupling proteins such as
353 UCP2 and UCP3 may elucidate whether the decreased efficiency is a byproduct or cause of
354 mitochondrial dysfunction, such as increased ΔΨm, in these cells. Our finding that cells with
355 DRP1 mutations have profound alterations in cristae morphology but apparent maintenance of
356 overall ATP production, raises the interesting possibility that DRP1 mutant cells have evolved
357 specialized mechanisms to cope with electron leakage and damaging reactive oxygen species. A
358 landmark study from Spinelli and collaborators demonstrated the ability of complex II to work in
359 reverse in some tissues with the intrinsic capacity to use fumarate as a terminal electron acceptor
360 (Spinelli et al., 2021). It is plausible that complex II reversal has evolved as a mechanism to
361 maintain mitochondrial function in cells with alterations in fission caused by DRP1 mutations.

362 The existence of two mechanistically and functionally distinct types of fission at the mitochondria
363 and the peroxisomes have not been clearly elucidated. In our study, we demonstrate that patient
364 fibroblasts with mutations in DRP1 also have elongated peroxisomal morphology. Previous
365 studies in mammalian cell culture revealed that peroxisome membrane elongation precedes
366 membrane constriction and final membrane fission (Delille et al., 2010; Schrader et al., 2016).
367 Whether peroxisomes have a specialized fusion machinery is still under debate. However, we
368 speculate that under particular metabolic conditions peroxisomes, particularly those in contact
369 with mitochondria, may be able to fuse to respond to cellular metabolic needs. Elongation of the
370 peroxisomes in various human disorders has been associated with alterations in fatty acid
371 oxidation (Waterham et al., 2016). However; in these cells, peroxisomal function cannot be fully
372 dissociated from changes in mitochondrial morphology. Our model (Figure 7) suggests that the
373 mechanistic and functional connection between peroxisome remodeling and metabolic
374 homeostasis could be dysregulated in mitochondrial diseases such EMPF1. We propose that in
375 this context, human diseases could provide insight into the causal mechanisms underlying basic
376 cellular processes, such as organelle fission. The detailed elucidation of DRP1-centric
377 mechanisms will reveal the connection between organelle dynamics and cell fate. Several
378 questions remain: Does stalling of mitochondrial fission affect the association/dissociation of other
379 proteins at point of fission? Is peripheral fission also inhibited in patient fibroblasts? If that is the
380 case, what are the consequences for mitophagy and mitochondrial DNA integrity? What are the
381 effects of peroxisomal elongation on fatty acid metabolism? How is cell division and mitochondrial
382 segregation affected by DRP1 mutations? How are cell fate transitions affected by DRP1
383 mutations? Answering these fundamental questions would provide insight into the mechanisms
384 of mitochondrial fission under the lens of this rare disease caused by dysregulated mitochondrial
385 and peroxisomal homeostasis, and inform the field on more rational and specific therapeutic
386 targets for these devastating neurodevelopmental disorders.

387 **STAR Methods**

388 **Cell Culture**

389 Human fibroblasts were thawed and plated directly in maintenance medium consisting of MEM
390 (Gibco #11095098) with 10% FBS (Sigma-Aldrich #F2442) and non-essential amino acids (Gibco
391 # 11-140-050). Cells were maintained at 37°C and 5% CO2 with media changes every other day.
392 Cells were passaged as needed using TrypLE (Thermo Fisher #12-064-013). For imaging
393 experiments, cells were re-plated onto #1.5 glass-bottom 35 mm dishes (Cellvis #D35C4-20-1.5-
394 N).

395 **Cell Treatments**

396 All treatments were added directly to fibroblasts in maintenance medium. The electron transport
397 chain decoupler CCCP (Sigma-Aldrich #C2759-250MG) was added to cells at a concentration of
398 1 μM. Cells were treated for 2 hours prior to fixation and imaging. All stock solutions were prepared
399 in DMSO.

400 **Plasmid Transfection**

401 Plasmid encoding mCherry-DRP1 (Addgene #49152) was transfected using FuGENE (Promega
402 #E2311) as described in the manufacturer protocol. Patient mutations were introduced to
403 plasmids using the In Fusion cloning kit (Takara Bio #638909) as described in the manufacturer
404 protocol. Cells were maintained until optimal transfection efficiency was reached before cells were
405 imaged.

406 **Immunofluorescence**

407 For immunofluorescence, cells were fixed with 4% paraformaldehyde for 20 min and
408 permeabilized in 1% Triton-X-100 for 10 min at room temperature. After blocking in 10% BSA,
409 cells were treated with primary and secondary antibodies using standard methods. Cells were
410 mounted in Fluoromount-G (Electron Microscopy Sciences #17984-25) prior to imaging. Primary

411 antibodies used include mouse anti-Mitochondria (Abcam #ab92824), rabbit anti-Tom20 (Cell
412 Signaling Technology #42406S), rabbit anti-DRP1 (Cell Signaling Technology #8570S), rabbit
413 anti-HSP60 (Cell Signaling Technologies # 12165S), mouse anti-PMP70 (Thermo Fisher # MA5-
414 31368), and rabbit anti-pDRP1 S616 (Cell Signaling Technology #3455S). Secondary antibodies
415 used include donkey anti-mouse Alexa Fluor-488 (Thermo Fisher Scientific #A21202), donkey
416 anti-rabbit Alexa Fluor-488 (Thermo Fisher Scientific #A21206), and donkey anti-mouse Alexa
417 Fluor-546 (Thermo Fisher Scientific #A10036), and donkey anti-rabbit Alexa Fluor-546 (Thermo
418 Fisher Scientific #A10040).

419 **Western Blot**

420 Gel samples were prepared by mixing cell lysates with LDS sample buffer (Life Technologies,
421 #NP0007) and 2-Mercaptoethanol (BioRad #1610710) and boiled at 95°C for 5 minutes. Samples
422 were resolved on 4-20% Mini-PROTEAN TGX precast gels (BioRad #4561096) and transferred
423 onto PVDF membrane (BioRad #1620177). Antibodies used for Western blotting are as follows:
424 rabbit anti-DRP-1 (Cell Signaling Technologies #8570S), rabbit anti-pDRP-1 S616 (Cell Signaling
425 Technologies #3455S), rabbit anti-OPA1 (Cell Signaling Technologies #67589S), mouse anti-
426 MFN1 (Abcam #ab57602, mouse anti-MFN2 (Abcam #ab56889), rabbit anti-MFF (Proteintech
427 #17090-1-AP), rabbit anti-MiD49 (Proteintech #16413-1-AP), rabbit anti-MiD51 (Proteintech
428 #20164-1-AP), and rabbit anti-FIS1 (Proteintech #10956-1-AP), and mouse anti-HSP70
429 (Invitrogen #MA3-006).

430 **Seahorse XF Analysis**

431 Fibroblasts were plated onto Seahorse XF96 V3 PS cell culture microplates 2 days before the
432 assay at 50,000 cells per well. One hour prior to the assay, media was switched to XF DMEM
433 media containing 1 mM pyruvate, 2 mM glutamine, and 10 mM glucose. For the Seahorse XF
434 Mito Stress Test, oxygen consumption rate (OCR) was measured sequentially after addition of
435 1.0 μM oligomycin, 0.5 μM FCCP, and 0.5 μM rotenone plus Antimycin A. Protein leak and

436 coupling efficiency were calculated using OCR. For the Seahorse XF Glycolytic Rate Assay, basal
437 glycolytic rate was measured by extracellular acidification, and compensatory glycolysis was
438 measured after addition of 0.5 μM rotenone plus antimycin A. Treatment with 50 mM 2-DG was
439 used as a negative control. For the Seahorse XF Fuel Flex Test, glutamine dependency was
440 measured by sequential addition of 3.0 μM BPTES followed by 4.0 μM Etomoxir plus 2.0 μM
441 UK5099. Fatty acid dependency was measured by sequential addition of 4.0 μM Etomoxir
442 followed by 3.0 μM BPTES plus 2.0 μM UK5099. Glucose dependency was measured by
443 sequential addition of 2.0 μM UK5099 followed by 3.0 μM BPTES plus 4.0 μM Etomoxir. For the
444 Seahorse XF Long Chain Fatty Acid Oxidation Stress Test, 24 hours prior to assay cells were
445 switched to base media containing 0.5 mM glucose, 1.0 mM glutamine, 0.5 mM XF L-carnitine,
446 and 1.0 % fetal bovine serum. One hour prior to the assay, media was switched to XF DMEM
447 media containing 2 mM glucose, 0.5 mM L-Carnitine, and Palmitate-BSA. Oxygen consumption
448 rate (OCR) was measured sequentially after addition of 4.0 μM etomoxir, 1.5 μM oligomycin, 2.0
449 μM FCCP, and 0.5 μM rotenone plus Antimycin A.

450 **RNA Extraction and cDNA Synthesis**

451 Cells were washed with PBS and scraped into 1000μl Trizol reagent. 200μl of chloroform was
452 added and the samples were incubated at room temperature for 5 minutes. The samples were
453 spun down at 12,000 g and the aqueous phase was collected. 500μl of isopropanol was added
454 to precipitate RNA and the sample was incubated for 25 minutes at room temperature, followed
455 by centrifugation at 12,000 g for 10 min at 4°C. The RNA pellet was washed with 75% ethanol,
456 semi-dried, and resuspended in 30μl of DEPC water. After quantification and adjusting the volume
457 of all the samples to 1μg/μl, the samples were treated with DNAse (New England Biolabs, #
458 M0303). 10μl of this volume was used to generate cDNA using the manufacturer's protocol
459 (Thermo Fisher, #4368814).

460 **Quantitative RT PCR (RT-qPCR)**

461 1ug of cDNA sample was used to run RT-qPCR for the primers mentioned in the table.
462 QuantStudio 3 Real-Time PCR machine, SYBR green master mix (Thermo Fisher, #4364346),
463 and manufacturer instructions were used to set up the assay.

464 **Image Acquisition**

465 Super-resolution images were acquired using a Nikon SIM microscope equipped with a 1.49 NA
466 100x Oil objective an Andor DU-897 EMCCD camera. Live-imaging experiments experiments
467 were acquired on a Nikon Eclipse Ti-E spinning disk confocal microscope equipped with a 1.40
468 NA 60X Oil objective and an Andor DU-897 EMCCD camera. Image processing and quantification
469 was performed using Fiji.

470 **Statistical Analysis**

471 All experiments were performed with a minimum of 3 biological replicates. Statistical significance
472 was determined by one-way or repeated measures ANOVA as appropriate for each experiment.
473 GraphPad Prism v8.1.2 was used for all statistical analysis and data visualization. Error bars in
474 all bar graphs represent standard error of the mean unless otherwise noted in the figure. No
475 outliers were removed from the analyses. Quantification of mitochondrial morphology was
476 performed in NIS-Elements (Nikon); briefly, we segmented mitochondria in 3D and performed
477 skeletonization of the resulting 3D mask. Skeleton major axis length, volume, and surface area
478 measurements were exported into Excel.

479 **Sample Preparation for Transmission Electron Microscope (TEM) Analysis**

480 Human fibroblasts were immediately washed in ice-cold saline. Samples were processed as
481 described by (Lam et. al., 2021, Pereira et al., 2017). Cells were fixed in 2.5% glutaraldehyde in
482 sodium cacodylate buffer for 1 hour at 37 °C, embedded in 2% agarose, postfixed in buffered 1%
483 osmium tetroxide, stained in 2% uranyl acetate, and dehydrated with an ethanol graded series.
484 After embedding in EMbed-812 resin, 80 nm sections were cut on an ultramicrotome and stained

485 with 2% uranyl acetate and lead citrate. Images were acquired on a JEOL JEM-1230
486 Transmission Electron Microscope, operating at 120 kV. Random images of human fibroblasts
487 were obtained.

488 **TEM Analysis**

489 Measurements of mitochondrial area, circularity, and length were performed using the multi-
490 measure region of interest (ROI) tool in ImageJ (Lam et. al., 2021, Parra et al., 2014). To measure
491 cristae morphology, we used ROIs in ImageJ to determine the cristae area, circulatory index,
492 number, volume, and cristae score. The NIH ImageJ software was used to manually trace and
493 analyze all mitochondria or cristae using the freehand told in the ImageJ application (Lam et. al.,
494 2021, Parra et al., 2014). To assign a mitochondrion a cristae score, cristae abundance and form
495 were evaluated. A score between 0 and 4 (0 – no sharply defined crista, 1 – greater than 50% of
496 mitochondrial area without cristae, 2 – greater than 25% of mitochondrial area without cristae, 3
497 – many cristae but irregular, 4 – many regular cristae) was assigned (Eisner et al., 2017).

498 **Serial Block Facing-Scanning Electron Microscopy (SBF-SEM) Processing**

499 Human fibroblasts were fixed in 2% glutaraldehyde in 0.1 M cacodylate buffer and processed
500 using a heavy metal protocol adapted from a previously published protocol (Courson et al., 2021;
501 Mustafi et al., 2014). Human fibroblasts were immersed in 3% potassium ferrocyanide and 2%
502 osmium tetroxide (1 hour at 4 °C), followed by filtered 0.1% thiocarbohydrazide (20 min), 2%
503 osmium tetroxide (30 min), and left overnight in 1% uranyl acetate at 4 °C (several de-ionized
504 H2O washes were performed between each step). The next day samples were immersed in a
505 0.6% lead aspartate solution (30 min at 60 °C and dehydrated in graded acetone (as described
506 for TEM). Human fibroblasts were impregnated with epoxy Taab 812 hard resin, embedded in
507 fresh resin, and polymerized at 60 °C for 36–48 hours. After polymerization, the block was
508 sectioned for TEM to identify the area of interest, then trimmed to 0.5 mm × 0.5 mm and glued to
509 an aluminum pin. The pin was placed into an FEI/Thermo Scientific Volumescope 2 scanning

510 electron microscope (SEM). The scope is a state-of-the-art SBF imaging system. For 3D EM
511 reconstruction, thin (0.09 μm) serial sections, 300 to 400 per block, were obtained from the blocks
512 that were processed for conventional TEM. Serial sections were collected onto formvar coated
513 slot grids (Pella, Redding CA), stained, and imaged, as described above. The segmentation of
514 SBF-SEM reconstructions was performed by manually tracing structural features through
515 sequential slices of the micrograph block. Images were collected from 30–50 serial sections,
516 which were then stacked, aligned, and visualized using Amira to make videos and quantify
517 volumetric structures.

518 **Statistical Analysis**

519 The results are presented as the mean ± standard error of the mean. Data were analyzed using
520 an unpaired T-test. If more than two groups were compared, one-way analysis of variance
521 (ANOVA) was performed, and significance was assessed using Fisher's protected least
522 significance difference test. GraphPad PRISM and Statplus software package was used for t-tests
523 and ANOVA analyses (SAS Institute: Cary, NC, USA). For all statistical analyses, a significant
524 difference was accepted when $P < 0.05$.

525 **Acknowledgements**

526 We would like to thank the patients and families for permission to publish this work. We thank Dr.
527 Eric Payne and Dr. Suzanne Hoppins for providing the patient-derived fibroblast lines used in this
528 paper. We would also like to thank Dr. Evan Krystofiak for providing EM expertise, and Dr.
529 Matthew Tyska, Dr. Uri Manor, and Dr. Kari Seedle, for providing advice and expertise with high-
530 resolution microscopy. This work was supported by 1R35 GM128915-01NIGMS (VG),
531 1RF1MH123971-01 (VG); the Precision Medicine and Mental Health Initiative sponsored by the
532 Vanderbilt Brain Institute (VG), 1R21CA227483-01A1NCI (VG), F99NS125829 (GLR), HHMI
533 Gilliam (GLR), and CBMS T32 (GLR). All SIM and spinning disk confocal microscopy imaging
534 and image analysis were performed in part through the use of the Vanderbilt Cell Imaging Shared

535 Resource, which is supported by NIH grants 1S10OD012324-01 and 1S10OD021630-01. The
536 authors declare no competing financial interests.

537 **Author Contributions**

538 G. Robertson and V. Gama conceived the study, designed experiments, interpreted data, and
539 wrote the manuscript. G. Robertson designed and carried out all the cell biology experiments,
540 with technical assistance from M. Patel and S. Riffle. J. Mears provided technical feedback and
541 insight into the conception and execution of study. A. Marshall, H. Beasley, Z. Vue, J. Shao, and
542 E. Garza Lopez performed the TEM, 3D EM and sbf-SEM experiments, quantification, and
543 analysis, supervised by A. Hinton.

544 **Figure Legends**

545 **Figure 1. DRP1 patient-derived fibroblasts have elongated mitochondrial morphology.** (A)
546 Representative images of mitochondrial morphology in patient-derived fibroblasts using
547 structured illumination microscopy (n=3, 7 cells per replicate). (B) Quantification of mitochondrial
548 volume, surface area, and major axis length. Analyzed using one-way ANOVA followed by
549 Dunnett's multiple comparison test. (C) Representative sbf-SEM 3D reconstructed images. Each
550 mitochondrion is colored a unique color. (D) Quantification of sbf-SEM for 3D mitochondrial
551 length, volume, and complexity index. Analyzed using one-way ANOVA followed by Dunnett's
552 multiple comparison test. (E) Representative images of mitochondrial morphology in control
553 fibroblasts transfected with either DRP1^{WT}-mCherry, DRP1^{G32A}-mCherry, or DRP1^{R403C}-mCherry
554 using structured illumination microscopy (n=3, 7 cells per replicate). (F) Quantification of
555 mitochondrial volume, surface area, and major axis length. Analyzed using one-way ANOVA
556 followed by Dunnett's multiple comparison test.

557 **Figure 2. Mutant G32A and R403C DRP1 are recruited to mitochondria. i.** (A) Western blot of
558 total protein lysate isolated from patient fibroblasts and probed for mitochondrial fusion proteins.

559 Representative image of three independent biological replicates. (B) Western blot of total protein
560 lysate isolated from patient fibroblasts and probed for mitochondrial fission proteins. Band density
561 is normalized to loading control (HSP70) and relative to control cells. Representative image of
562 three independent biological replicates. (C) Representative images of mitochondrial and DRP1 in
563 patient-derived fibroblasts using structured illumination microscopy (n=3, 7 cells per replicate).
564 Top image is a zoom of white box from bottom image. (D) Quantification of DRP1 puncta that
565 overlap with mitochondria and volume of DRP1 puncta. Analyzed using one-way ANOVA followed
566 by Dunnett's multiple comparison test. (E) Representative images of mitochondrial morphology in
567 patient-derived fibroblasts treated with either DMSO or CCCP for 1 hours using structured
568 illumination microscopy (n=3, 7 cells per replicate). (F) Quantification of mitochondrial volume,
569 surface area, and major axis length. Analyzed using one-way ANOVA followed by Dunnett's
570 multiple comparison test.

571 **Figure 3. Mitochondrial defects lead to inefficient coupling of the electron transport chain**
572 **and higher glycolytic rate.** (A) Oxygen consumption rate and extracellular acidification rate in
573 patient fibroblasts as measured using Seahorse Mitochondrial stress test (n=3, 20 wells per
574 replicate). Oligomycin applied at 20 minutes, FCCP applied at 40 minutes, and
575 rotenone/Antimycin A applied at 60 minutes. Analyzed using two-way ANOVA followed by Šídák's
576 multiple comparisons test. (B) Proton leak and coupling efficiency calculated using oxygen
577 consumption rate. (C) Basal glycolysis of patient fibroblasts measure using Seahorse Glycolytic
578 Rate Assay. Compensatory glycolysis measured following application of rotenone/Antimycin A.
579 (D) Glucose, glutamine, and fatty acid dependency of the electron transport chain measured using
580 Seahorse Fuel Flex Assay. Glucose dependency measured after application of UK5099,
581 glutamine dependency measured after application of BPTES, and fatty acid dependency measure
582 after application of Etomoxir. (E) qRT-PCR analysis of gene expression in fibroblasts relative to
583 control and normalized to two housekeeping genes (*GPI* and *GAPDH)*. Quantifications are shown

584 for three independent biological replicates. (F) Western blot of total protein lysate isolated from
585 patient fibroblasts and probed for mitochondrial pyruvate carriers. Band density is normalized to
586 loading control (HSP70) and relative to control cells. Representative image of three independent
587 biological replicates.

588 **Figure 4. DRP1 patient fibroblasts have more hyperpolarized mitochondrial membrane**
589 **potential.** (A) Representative live-cell imaging of patient-derived fibroblasts treated with 500nM
590 TMRE for 10 minutes. Cells were imaged every 15 seconds for 15 minutes using spinning disk
591 confocal (n=3, 7 cells per replicate). Scale bar: 5 µm.

592 **Figure 5. Cristae morphology is altered in patient cells.** (A) Transmission electron microscopy
593 of patient fibroblasts. 3 representative images per line shown. (B) Quantification of cristae from
594 TEM images for cristae score and cristae number relative to mitochondrial length. Analyzed using
595 one-way ANOVA followed by Dunnett's multiple comparison test.

596 **Figure 6. Patient fibroblasts have elongated peroxisomes.** (A) Representative images of
597 peroxisomal morphology in patient-derived fibroblasts using structured illumination microscopy
598 (n=3, 7 cells per replicate). (B) Quantification of peroxisomal volume, surface area, and major
599 axis length. Analyzed using one-way ANOVA followed by Dunnett's multiple comparison test. (C)
600 qRT-PCR analysis of gene expression in fibroblasts relative to control and normalized to two
601 housekeeping genes (*GPI* and *GAPDH)*. Quantifications are shown for three independent
602 biological replicates. (D) Oxygen consumption rate in patient fibroblasts as measured using
603 Seahorse Analyzer XFe96 (n=3, 20 wells per replicate). Etomoxir applied after 20 minutes,
604 oligomycin applied at 40 minutes, FCCP applied at 60 minutes, and rotenone/Antimycin A applied
605 at 80 minutes. Analyzed using two-way ANOVA followed by Šídák's multiple comparisons test.

606 **Figure 7: Current model of the cellular responses to EMPF1 associated DRP1 mutations.**
607 EMPF1- associated mutations do not appear to alter the capacity of DRP1 to be recruited to points

608 of fission, but rather cause stalling of the fission events. Pausing peroxisomal and mitochondrial
609 fission results in alterations of cristae structure, changes in mitochondrial membrane potential,
610 decreased mitochondrial coupling efficiency, delayed cell death response, and overall metabolic
611 adaptations.

612 **References**

613 Afzal N, Lederer WJ, Jafri MS, Mannella CA. 2021. Effect of crista morphology on mitochondrial
614 ATP output: A computational study. *Curr Res Physiol* **4**:163–176.
615 doi:10.1016/J.CRPHYS.2021.03.005

616 Alexander C, Votruba M, Pesch UEA, Thiselton DL, Mayer S, Moore A, Rodriguez M, Kellner U,
617 Leo-Kottler B, Auburger G, Bhattacharya SS, Wissinger B. 2000. OPA1, encoding a
618 dynamin-related GTPase, is mutated in autosomal dominant optic atrophy linked to
619 chromosome 3q28. *Nat Genet 2000 262* **26**:211–215. doi:10.1038/79944

620 Bayraktar EC, Baudrier L, Özerdem C, Lewis CA, Chan SH, Kunchok T, Abu-Remaileh M,
621 Cangelosi AL, Sabatini DM, Birsoy K, Chen WW. 2019. MITO-Tag Mice enable rapid
622 isolation and multimodal profiling of mitochondria from specific cell types in vivo. *Proc Natl*
623 *Acad Sci U S A* **116**:303–312. doi:10.1073/pnas.1816656115

624 Bricker DK, Taylor EB, Schell JC, Orsak T, Boutron A, Chen YC, Cox JE, Cardon CM, Van
625 Vranken JG, Dephoure N, Redin C, Boudina S, Gygi SP, Brivet M, Thummel CS, Rutter J.
626 2012. A mitochondrial pyruvate carrier required for pyruvate uptake in yeast, Drosophila, and
627 humans. *Science* **337**:96–100. doi:10.1126/SCIENCE.1218099

628 Chakrabarti R, Ji WK, Stan R V., Sanz J de J, Ryan TA, Higgs HN. 2018. INF2-mediated actin
629 polymerization at the ER stimulates mitochondrial calcium uptake, inner membrane
630 constriction, and division. *J Cell Biol* **217**:251–268. doi:10.1083/JCB.201709111

631 Chandel NS. 2021. Lipid Metabolism. *Cold Spring Harb Perspect Biol* **13**.
632 doi:10.1101/CSHPERSPECT.A040576

633 Chang C, Blackstone C. 2007. Drp1 phosphorylation and mitochondrial regulation. *EMBO Rep*
634 **8**:1088–1089. doi:10.1038/sj.embor.7401118

635 Chao YH, Robak LA, Xia F, Koenig MK, Adesina A, Bacino CA, Scaglia F, Bellen HJ, Wangler
636 MF. 2016. Missense variants in the middle domain of DNM1L in cases of infantile
637 encephalopathy alter peroxisomes and mitochondria when assayed in Drosophila. *Hum Mol*
638 *Genet* **25**:1846–1856. doi:10.1093/HMG/DDW059

639 Chen H, Detmer SA, Ewald AJ, Griffin EE, Fraser SE, Chan DC. 2003. Mitofusins Mfn1 and Mfn2
640 coordinately regulate mitochondrial fusion and are essential for embryonic development. *J*
641 *Cell Biol* **160**:189–200. doi:10.1083/JCB.200211046

642 Cogliati S, Frezza C, Soriano ME, Varanita T, Quintana-Cabrera R, Corrado M, Cipolat S, Costa
643 V, Casarin A, Gomes LC, Perales-Clemente E, Salviati L, Fernandez-Silva P, Enriquez JA,
644 Scorrano L. 2013. Mitochondrial Cristae Shape Determines Respiratory Chain
645 Supercomplexes Assembly and Respiratory Efficiency. *Cell* **155**:160–171.
646 doi:10.1016/J.CELL.2013.08.032

647 Csordás G, Renken C, Várnai P, Walter L, Weaver D, Buttle KF, Balla T, Mannella CA, Hajnóczky
648 G. 2006. Structural and functional features and significance of the physical linkage between
649 ER and mitochondria. *J Cell Biol* **174**:915–921. doi:10.1083/jcb.200604016

650 Davies KM, Strauss M, Daum B, Kief JH, Osiewacz HD, Rycovska A, Zickermann V, Kühlbrandt
651 W. 2011. Macromolecular organization of ATP synthase and complex I in whole
652 mitochondria. *Proc Natl Acad Sci U S A* **108**:14121–14126.
653 doi:10.1073/PNAS.1103621108/-/DCSUPPLEMENTAL

654 Delettre C, Lenaers G, Griffoin JM, Gigarel N, Lorenzo C, Belenguer P, Pelloquin L, Grosgeorge
655 J, Turc-Carel C, Perret E, Astarie-Dequeker C, Lasquellec L, Arnaud B, Ducommun B,
656 Kaplan J, Hamel CP. 2000. Nuclear gene OPA1, encoding a mitochondrial dynamin-related
657 protein, is mutated in dominant optic atrophy. *Nat Genet 2000 262* **26**:207–210.
658 doi:10.1038/79936

659 Delille HK, Agricola B, Guimaraes SC, Borta H, Lüers GH, Fransen M, Schrader M. 2010.
660 Pex11pbeta-mediated growth and division of mammalian peroxisomes follows a maturation
661 pathway. *J Cell Sci* **123**:2750–2762. doi:10.1242/JCS.062109

662 Ding L, Sun W, Balaz M, He A, Klug M, Wieland S, Caiazzo R, Raverdy V, Pattou F, Lefebvre P,
663 Lodhi IJ, Staels B, Heim M, Wolfrum C. 2021. Peroxisomal β-oxidation acts as a sensor for
664 intracellular fatty acids and regulates lipolysis. *Nat Metab* **3**:1648–1661.
665 doi:10.1038/S42255-021-00489-2

666 Dorn GW. 2015. Mitochondrial dynamism and heart disease: changing shape and shaping
667 change. *EMBO Mol Med* **7**:865–877. doi:10.15252/emmm.201404575

668 Eisner V, Cupo RR, Gao E, Csordás G, Slovinsky WS, Paillard M, Cheng L, Ibetti J, Chen SRW,
669 Chuprun JK, Hoek JB, Koch WJ, Hajnóczky G. 2017. Mitochondrial fusion dynamics is robust
670 in the heart and depends on calcium oscillations and contractile activity. *Proc Natl Acad Sci*
671 *U S A* **114**:E859–E868. doi:10.1073/PNAS.1617288114/-/DCSUPPLEMENTAL

672 Eramo MJ, Lisnyak V, Formosa LE, Ryan MT. 2020. The “mitochondrial contact site and cristae
673 organising system” (MICOS) in health and human disease. *J Biochem* **167**:243–255.
674 doi:10.1093/JB/MVZ111

675 Fahrner JA, Liu R, Perry MS, Klein J, Chan DC. 2016. A novel de novo dominant negative
676 mutation in DNM1L impairs mitochondrial fission and presents as childhood epileptic
677 encephalopathy. *Am J Med Genet A* **170**:2002–2011. doi:10.1002/AJMG.A.37721

678 Faitg J, Lacefield C, Davey T, White K, Laws R, Kosmidis S, Reeve AK, Kandel ER, Vincent AE,
679 Picard M. 2021. 3D neuronal mitochondrial morphology in axons, dendrites, and somata of
680 the aging mouse hippocampus. *Cell Rep* **36**.
681 doi:10.1016/J.CELREP.2021.109509/ATTACHMENT/28BF2465-59D0-4B68-BCDD-
682 D3F180754B5F/MMC1.PDF

683 Fan J, Li X, Issop L, Culty M, Papadopoulos V. 2016. ACBD2/ECI2-Mediated Peroxisome-
684 Mitochondria Interactions in Leydig Cell Steroid Biosynthesis. *Mol Endocrinol* **30**:763–782.
685 doi:10.1210/ME.2016-1008

686 Ferreira AR, Marques M, Ramos B, Kagan JC, Ribeiro D. 2021. Emerging roles of peroxisomes
687 in viral infections. *Trends Cell Biol*. doi:10.1016/J.TCB.2021.09.010

688 Fonseca TB, Sánchez-Guerrero Á, Milosevic I, Raimundo N. 2019. Mitochondrial fission requires
689 DRP1 but not dynamins. *Nature*. doi:10.1038/s41586-019-1296-y

690 Forkink M, Manjeri GR, Liemburg-Apers DC, Nibbeling E, Blanchard M, Wojtala A, Smeitink JAM,
691 Wieckowski MR, Willems PHGM, Koopman WJH. 2014. Mitochondrial hyperpolarization
692 during chronic complex I inhibition is sustained by low activity of complex II, III, IV and V.
693 *Biochim Biophys Acta - Bioenerg* **1837**:1247–1256. doi:10.1016/J.BBABIO.2014.04.008

694 Fransen M, Lismont C, Walton P. 2017. The Peroxisome-Mitochondria Connection: How and
695 Why? *Int J Mol Sci* **18**. doi:10.3390/IJMS18061126

696 Friedman JR, Lackner LL, West M, DiBenedetto JR, Nunnari J, Voeltz GK. 2011. ER tubules mark
697 sites of mitochondrial division. *Science (80-)* **334**:358–362.
698 doi:10.1126/SCIENCE.1207385/SUPPL_FILE/FRIEDMAN.SOM.REV1.PDF

699 Fröhlich C, Grabiger S, Schwefel D, Faelber K, Rosenbaum E, Mears J, Rocks O, Daumke O.
700 2013. Structural insights into oligomerization and mitochondrial remodelling of dynamin 1-
701 like protein. *EMBO J* **32**:1280–1292. doi:10.1038/EMBOJ.2013.74

702 Gandre-Babbe S, Van Der Bliek AM. 2008. The novel tail-anchored membrane protein Mff
703 controls mitochondrial and peroxisomal fission in mammalian cells. *Mol Biol Cell* **19**:2402–
704 2412. doi:10.1091/MBC.E07-12-
705 1287/ASSET/IMAGES/LARGE/ZMK0060885640008.JPEG

706 Garza-Lopez E, Vue Z, Katti P, Neikirk K, Biete M, Lam J, Beasley HK, Marshall AG, Rodman
707 TA, Christensen TA, Salisbury JL, Vang L, Mungai M, AshShareef S, Murray SA, Shao J,
708 Streeter J, Glancy B, Pereira RO, Dale Abel E, Hinton A, Jr, Lopez G. 2021. Protocols for
709 Generating Surfaces and Measuring 3D Organelle Morphology Using Amira. *Cells 2022, Vol*
710 *11, Page 65* **11**:65. doi:10.3390/CELLS11010065

711 Hatch AL, Gurel PS, Higgs HN. 2014. Novel roles for actin in mitochondrial fission. *J Cell Sci*
712 **127**:4549–4560. doi:10.1242/JCS.153791

713 Hatch AL, Ji WK, Merrill RA, Strack S, Higgs HN. 2016. Actin filaments as dynamic reservoirs for
714 Drp1 recruitment. *Mol Biol Cell* **27**:3109–3121. doi:10.1091/MBC.E16-03-0193

715 Herzig S, Raemy E, Montessuit S, Veuthey JL, Zamboni N, Westermann B, Kunji ERS, Martinou
716 JC. 2012. Identification and functional expression of the mitochondrial pyruvate carrier.
717 *Science* **337**:93–96. doi:10.1126/SCIENCE.1218530

718 Ishihara N, Nomura M, Jofuku A, Kato H, Suzuki SO, Masuda K, Otera H, Nakanishi Y, Nonaka
719 I, Goto YI, Taguchi N, Morinaga H, Maeda M, Takayanagi R, Yokota S, Mihara K. 2009.
720 Mitochondrial fission factor Drp1 is essential for embryonic development and synapse
721 formation in mice. *Nat Cell Biol* **11**:958–966. doi:10.1038/ncb1907

722 Itoyama A, Michiyuki S, Honsho M, Yamamoto T, Moser A, Yoshida Y, Fujiki Y. 2013. Mff
723 functions with Pex11pβ and DLP1 in peroxisomal fission. *Biol Open* **2**:998.
724 doi:10.1242/BIO.20135298

725 Iwata R, Casimir P, Vanderhaeghen P. 2020. Mitochondrial dynamics in postmitotic cells regulate
726 neurogenesis. *Science (80-)* **369**:858–862. doi:10.1126/science.aba9760

727 Ji WK, Chakrabarti R, Fan X, Schoenfeld L, Strack S, Higgs HN. 2017. Receptor-mediated Drp1
728 oligomerization on endoplasmic reticulum. *J Cell Biol* **216**:4123–4139.

729 doi:10.1083/JCB.201610057

730 Ji WK, Hatch AL, Merrill RA, Strack S, Higgs HN. 2015. Actin filaments target the oligomeric
731 maturation of the dynamin GTPase Drp1 to mitochondrial fission sites. *Elife* **4**.
732 doi:10.7554/eLife.11553

733 Kamerkar SC, Kraus F, Sharpe AJ, Pucadyil TJ, Ryan MT. 2018. Dynamin-related protein 1 has
734 membrane constricting and severing abilities sufficient for mitochondrial and peroxisomal
735 fission. *Nat Commun* **9**:1–15. doi:10.1038/s41467-018-07543-w

736 Keller N, Paketci C, Edem P, Thiele H, Yis U, Wirth B, Karakaya M. 2021. De novo DNM1L variant
737 presenting with severe muscular atrophy, dystonia and sensory neuropathy. *Eur J Med*
738 *Genet* **64**. doi:10.1016/J.EJMG.2020.104134

739 Khacho M, Clark A, Svoboda DS, Azzi J, MacLaurin JG, Meghaizel C, Sesaki H, Lagace DC,
740 Germain M, Harper ME, Park DS, Slack RS. 2016. Mitochondrial Dynamics Impacts Stem
741 Cell Identity and Fate Decisions by Regulating a Nuclear Transcriptional Program. *Cell Stem*
742 *Cell* **19**:232–247. doi:10.1016/j.stem.2016.04.015

743 King WT, Axelrod CL, Zunica ERM, Noland RC, Davuluri G, Fujioka H, Tandler B, Pergola K,
744 Hermann GE, Rogers RC, López-Domènech S, Dantas WS, Stadler K, Hoppel CL, Kirwan
745 JP. 2021. Dynamin-related protein 1 regulates substrate oxidation in skeletal muscle by
746 stabilizing cellular and mitochondrial calcium dynamics. *J Biol Chem* **297**:101196.
747 doi:10.1016/J.JBC.2021.101196

748 Kleele T, Rey T, Winter J, Zaganelli S, Mahecic D, Perreten Lambert H, Ruberto FP, Nemir M,
749 Wai T, Pedrazzini T, Manley S. 2021. Distinct fission signatures predict mitochondrial
750 degradation or biogenesis. *Nature* **593**:435–439. doi:10.1038/S41586-021-03510-6

751 Koch A, Thiemann M, Grabenbauer M, Yoon Y, McNiven MA, Schrader M. 2003. Dynamin-like

752 protein 1 is involved in peroxisomal fission. *J Biol Chem* **278**:8597–8605.
753 doi:10.1074/JBC.M211761200

754 Koch J, Brocard C. 2012. PEX11 proteins attract Mff and human Fis1 to coordinate peroxisomal
755 fission. *J Cell Sci* **125**:3813–3826. doi:10.1242/JCS.102178/263234/AM/PEX11-
756 PROTEINS-ATTRACT-MFF-AND-HFIS1-TO-COORDINATE

757 Kondadi AK, Anand R, Hänsch S, Urbach J, Zobel T, Wolf DM, Segawa M, Liesa M, Shirihai OS,
758 Weidtkamp-Peters S, Reichert AS. 2020. Cristae undergo continuous cycles of membrane
759 remodelling in a MICOS-dependent manner. *EMBO Rep* **21**:e49776.
760 doi:10.15252/EMBR.201949776

761 Lam J, Katti P, Biete M, Mungai M, Ashshareef S, Neikirk K, Lopez EG, Vue Z, Christensen TA,
762 Beasley HK, Rodman TA, Murray SA, Salisbury JL, Glancy B, Shao J, Pereira RO, Abel ED,
763 Hinton, A., Jr. 2021. A Universal Approach to Analyzing Transmission Electron Microscopy
764 with ImageJ. *Cells 2021, Vol 10, Page 2177* **10**:2177. doi:10.3390/CELLS10092177

765 Lee YJ, Jeong SY, Karbowski M, Smith CL, Youle RJ. 2004. Roles of the mammalian
766 mitochondrial fission and fusion mediators Fis1, Drp1, and Opa1 in apoptosis. *Mol Biol Cell*
767 **15**:5001–5011. doi:10.1091/MBC.E04-04-0294

768 Lewis SC, Uchiyama LF, Nunnari J. 2016. ER-mitochondria contacts couple mtDNA synthesis
769 with Mitochondrial division in human cells. *Science (80-)* **353**.
770 doi:10.1126/SCIENCE.AAF5549

771 Li L, Conradson DM, Bharat V, Kim MJ, Hsieh CH, Minhas PS, Papakyrikos AM, Durairaj AS,
772 Ludlam A, Andreasson KI, Partridge L, Cianfrocco MA, Wang X. 2021. A mitochondrial
773 membrane-bridging machinery mediates signal transduction of intramitochondrial oxidation.
774 *Nat Metab* **3**:1242–1258. doi:10.1038/S42255-021-00443-2

775 Li S, Xu S, Roelofs BA, Boyman L, Jonathan Lederer W, Sesaki H, Karbowski M. 2015. Transient
776 assembly of F-actin on the outer mitochondrial membrane contributes to mitochondrial
777 fission. *J Cell Biol* **208**:109–123. doi:10.1083/jcb.201404050

778 Liu Xingmiao, Zhang Z, Li D, Lei M, Li Q, Liu Xiaojun, Zhang P. 2021. DNM1L-Related
779 Mitochondrial Fission Defects Presenting as Encephalopathy: A Case Report and Literature
780 Review. *Front Pediatr* **9**. doi:10.3389/FPED.2021.626657

781 Lodhi IJ, Semenkovich CF. 2014. Peroxisomes: a nexus for lipid metabolism and cellular
782 signaling. *Cell Metab* **19**:380–392. doi:10.1016/J.CMET.2014.01.002

783 Longo F, Benedetti S, Zambon AA, Sora MGN, Di Resta C, De Ritis D, Quattrini A, Maltecca F,
784 Ferrari M, Previtali SC. 2020. Impaired turnover of hyperfused mitochondria in severe axonal
785 neuropathy due to a novel DRP1 mutation. *Hum Mol Genet* **29**:177–188.
786 doi:10.1093/HMG/DDZ211

787 Losó n OC, Song Z, Chen H, Chan DC. 2013. Fis1, Mff, MiD49, and MiD51 mediate Drp1
788 recruitment in mitochondrial fission. *Mol Biol Cell* **24**:659–667. doi:10.1091/MBC.E12-10-
789 0721

790 Martinou JC, Youle RJ. 2006. Which came first, the cytochrome c release or the mitochondrial
791 fission? *Cell Death Differ* **13**:1291–1295. doi:10.1038/SJ.CDD.4401985

792 Montecinos-Franjola F, Bauer BL, Mears JA, Ramachandran R. 2020. GFP fluorescence tagging
793 alters dynamin-related protein 1 oligomerization dynamics and creates disassembly-
794 refractory puncta to mediate mitochondrial fission. *Sci Reports 2020 101* **10**:1–16.
795 doi:10.1038/s41598-020-71655-x

796 Nagashima S, Tábara LC, Tilokani L, Paupe V, Anand H, Pogson JH, Zunino R, McBride HM,
797 Prudent J. 2020. Golgi-derived PI(4)P-containing vesicles drive late steps of mitochondrial

division. *Science (80-)* **367**:1366–1371. doi:10.1126/science.aax6089

Nasca A, Legati A, Baruffini E, Nolli C, Moroni I, Ardissone A, Goffrini P, Ghezzi D. 2016. Biallelic Mutations in DNM1L are Associated with a Slowly Progressive Infantile Encephalopathy. *Hum Mutat* **37**:898–903. doi:10.1002/HUMU.23033

Nolan DA, Chen B, Michon AM, Salatka E, Arndt D. 2019. A Rasmussen encephalitis, autoimmune encephalitis, and mitochondrial disease mimicker: expanding the *DNM1L*-associated intractable epilepsy and encephalopathy phenotype. *Epileptic Disord* **21**:112–116. doi:10.1684/EPD.2019.1036

Osellame LD, Singh AP, Stroud DA, Palmer CS, Stojanovski D, Ramachandran R, Ryan MT. 2016. Cooperative and independent roles of the Drp1 adaptors Mff, MiD49 and MiD51 in mitochondrial fission. *J Cell Sci* **129**:2170–2181. doi:10.1242/JCS.185165/-/DC1

Otera H, Miyata N, Kuge O, Mihara K. 2016. Drp1-dependent mitochondrial fission via MiD49/51 is essential for apoptotic cristae remodeling. *J Cell Biol* **212**:531–544. doi:10.1083/jcb.201508099

Palmer CS, Elgass KD, Parton RG, Osellame LD, Stojanovski D, Ryan MT. 2013. Adaptor proteins MiD49 and MiD51 can act independently of Mff and Fis1 in Drp1 recruitment and are specific for mitochondrial fission. *J Biol Chem* **288**:27584–27593. doi:10.1074/JBC.M113.479873

Prigione A, Adjaye J. 2011. Modulation of mitochondrial biogenesis and bioenergetic metabolism upon in vitro and in vivo differentiation of human ES and iPS cells. *Int J Dev Biol*. doi:10.1387/ijdb.103198ap

Rasmussen ML, Taneja N, Neininger AC, Wang L, Robertson GL, Riffle SN, Shi L, Knollmann BC, Burnette DT, Gama V. 2020. MCL-1 Inhibition by Selective BH3 Mimetics Disrupts

821 Mitochondrial Dynamics Causing Loss of Viability and Functionality of Human
822 Cardiomyocytes. *iScience* **23**. doi:10.1016/j.isci.2020.101015

823 Ravi A, Palamiuc L, Loughran RM, Triscott J, Arora GK, Kumar A, Tieu V, Pauli C, Reist M, Lew
824 RJ, Houlihan SL, Fellmann C, Metallo C, Rubin MA, Emerling BM. 2021. PI5P4Ks drive
825 metabolic homeostasis through peroxisome-mitochondria interplay. *Dev Cell* **56**:1661-
826 1676.e10. doi:10.1016/J.DEVCEL.2021.04.019

827 Ryan CS, Fine AL, Cohen AL, Schiltz BM, Renaud DL, Wirrell EC, Patterson MC, Boczek NJ, Liu
828 R, Babovic-Vuksanovic D, Chan DC, Payne ET. 2018. De Novo DNM1L Variant in a
829 Teenager With Progressive Paroxysmal Dystonia and Lethal Super-refractory Myoclonic
830 Status Epilepticus. *J Child Neurol* **33**:651–658. doi:10.1177/0883073818778203

831 Schrader M, Costello JL, Godinho LF, Azadi AS, Islinger M. 2016. Proliferation and fission of
832 peroxisomes - An update. *Biochim Biophys Acta* **1863**:971–983.
833 doi:10.1016/J.BBAMCR.2015.09.024

834 Schrader M, Kamoshita M, Islinger M. 2020. Organelle interplay-peroxisome interactions in health
835 and disease. *J Inherit Metab Dis* **43**:71–89. doi:10.1002/JIMD.12083

836 Sheffer R, Douiev L, Edvardson S, Shaag A, Tamimi K, Soiferman D, Meiner V, Saada A. 2016.
837 Postnatal microcephaly and pain insensitivity due to a de novo heterozygous DNM1L
838 mutation causing impaired mitochondrial fission and function. *Am J Med Genet Part A*
839 **170**:1603–1607. doi:10.1002/AJMG.A.37624

840 Smaili SS, Hsu YT, Sanders KM, Russell JT, Youle RJ. 2001. Bax translocation to mitochondria
841 subsequent to a rapid loss of mitochondrial membrane potential. *Cell Death Differ* **8**:909–
842 920. doi:10.1038/SJ.CDD.4400889

843 Smirnova E, Griparic L, Shurland DL, van der Bliek AM. 2001. Dynamin-related protein Drp1 is

required for mitochondrial division in mammalian cells. *Mol Biol Cell* **12**:2245–56. doi:10.1091/mbc.12.8.2245

Spinelli JB, Rosen PC, Sprenger H-G, Puszynska AM, Mann JL, Roessler JM, Cangelosi AL, Henne A, Condon KJ, Zhang T, Kunchok T, Lewis CA, Chandel NS, Sabatini DM. 2021. Fumarate is a terminal electron acceptor in the mammalian electron transport chain. *Science* **374**:1227–1237. doi:10.1126/SCIENCE.ABI7495

Sugiura A, Mattie S, Prudent J, Mcbride HM. 2017. Newly born peroxisomes are a hybrid of mitochondrial and ER-derived pre-peroxisomes. *Nature* **542**:251–254. doi:10.1038/NATURE21375

Taguchi N, Ishihara N, Jofuku A, Oka T, Mihara K. 2007. Mitotic phosphorylation of dynamin-related GTPase Drp1 participates in mitochondrial fission. *J Biol Chem* **282**:11521–11529. doi:10.1074/jbc.M607279200

Tanaka H, Okazaki T, Aoyama S, Yokota M, Koike M, Okada Y, Fujiki Y, Gotoh Y. 2019. Peroxisomes control mitochondrial dynamics and the mitochondrion-dependent apoptosis pathway. *J Cell Sci* **132**. doi:10.1242/JCS.224766

Valera-Alberni M, Joffraud M, Miro-Blanch J, Capellades J, Junza A, Dayon L, Núñez Galindo A, Sanchez-Garcia JL, Valsesia A, Cercillieux A, Söllner F, Ladurner AG, Yanes O, Cantó C. 2021. Crosstalk between Drp1 phosphorylation sites during mitochondrial remodeling and their impact on metabolic adaptation. *Cell Rep* **36**. doi:10.1016/J.CELREP.2021.109565/ATTACHMENT/3EF18C2E-C1FE-434A-A87F-E1E1BD407021/MMC1.PDF

Vandeleur D, Chen C V., Huang EJ, Connolly AJ, Sanchez H, Moon-Grady AJ. 2019. Novel and lethal case of cardiac involvement in DNM1L mitochondrial encephalopathy. *Am J Med Genet Part A* **179**:2486–2489. doi:10.1002/AJMG.A.61371

868 Vantaggiato C, Castelli M, Giovarelli M, Orso G, Bassi MT, Clementi E, De Palma C. 2019. The
869 Fine Tuning of Drp1-Dependent Mitochondrial Remodeling and Autophagy Controls
870 Neuronal Differentiation. *Front Cell Neurosci* **13**:120. doi:10.3389/fncel.2019.00120

871 Vincent AE, White K, Davey T, Philips J, Ogden RT, Lawess C, Warren C, Hall MG, Ng YS,
872 Falkous G, Holden T, Deehan D, Taylor RW, Turnbull DM, Picard M. 2019. Quantitative 3D
873 Mapping of the Human Skeletal Muscle Mitochondrial Network. *Cell Rep* **26**:996-1009.e4.
874 doi:10.1016/J.CELREP.2019.01.010/ATTACHMENT/FB7711C2-65A0-4155-8EB8-
875 6FD4440E627D/MMC1.PDF

876 Wai T, Langer T. 2016. Mitochondrial Dynamics and Metabolic Regulation. *Trends Endocrinol*
877 *Metab*. doi:10.1016/j.tem.2015.12.001

878 Wakabayashi J, Zhang Z, Wakabayashi N, Tamura Y, Fukaya M, Kensler TW, Iijima M, Sesaki
879 H. 2009. The dynamin-related GTPase Drp1 is required for embryonic and brain
880 development in mice. *J Cell Biol* **186**:805–816. doi:10.1083/jcb.200903065

881 Wasiak S, Zunino R, McBride HM. 2007. Bax/Bak promote sumoylation of DRP1 and its stable
882 association with mitochondria during apoptotic cell death. *J Cell Biol* **177**:439–450.
883 doi:10.1083/JCB.200610042

884 Wasilewski M, Chacinska A. 2021. MIC60 relays oxidation to block mitophagy. *Nat Metab 2021*
885 *39* **3**:1146–1147. doi:10.1038/s42255-021-00460-1

886 Waterham HR, Ferdinandusse S, Wanders RJA. 2016. Human disorders of peroxisome
887 metabolism and biogenesis. *Biochim Biophys Acta - Mol Cell Res* **1863**:922–933.
888 doi:10.1016/J.BBAMCR.2015.11.015

889 Waterham HR, Koster J, van Roermund CWT, Mooyer PAW, Wanders RJA, Leonard J V. 2007.
890 A lethal defect of mitochondrial and peroxisomal fission. *N Engl J Med* **356**:1736–1741.

891 doi:10.1056/NEJMOA064436

892 Whitley BN, Lam C, Cui H, Haude K, Bai R, Escobar L, Hamilton A, Brady L, Tarnopolsky MA,
893 Dengle L, Picker J, Lincoln S, Lackner LL, Glass IA, Hoppins S. 2018. Aberrant Drp1-
894 mediated mitochondrial division presents in humans with variable outcomes. *Hum Mol Genet*
895 **27**:3710–3719. doi:10.1093/hmg/ddy287

896 Wilkens V, Kohl W, Busch K. 2013. Restricted diffusion of OXPHOS complexes in dynamic
897 mitochondria delays their exchange between cristae and engenders a transitory mosaic
898 distribution. *J Cell Sci* **126**:103–116. doi:10.1242/JCS.108852

899

Figure 1

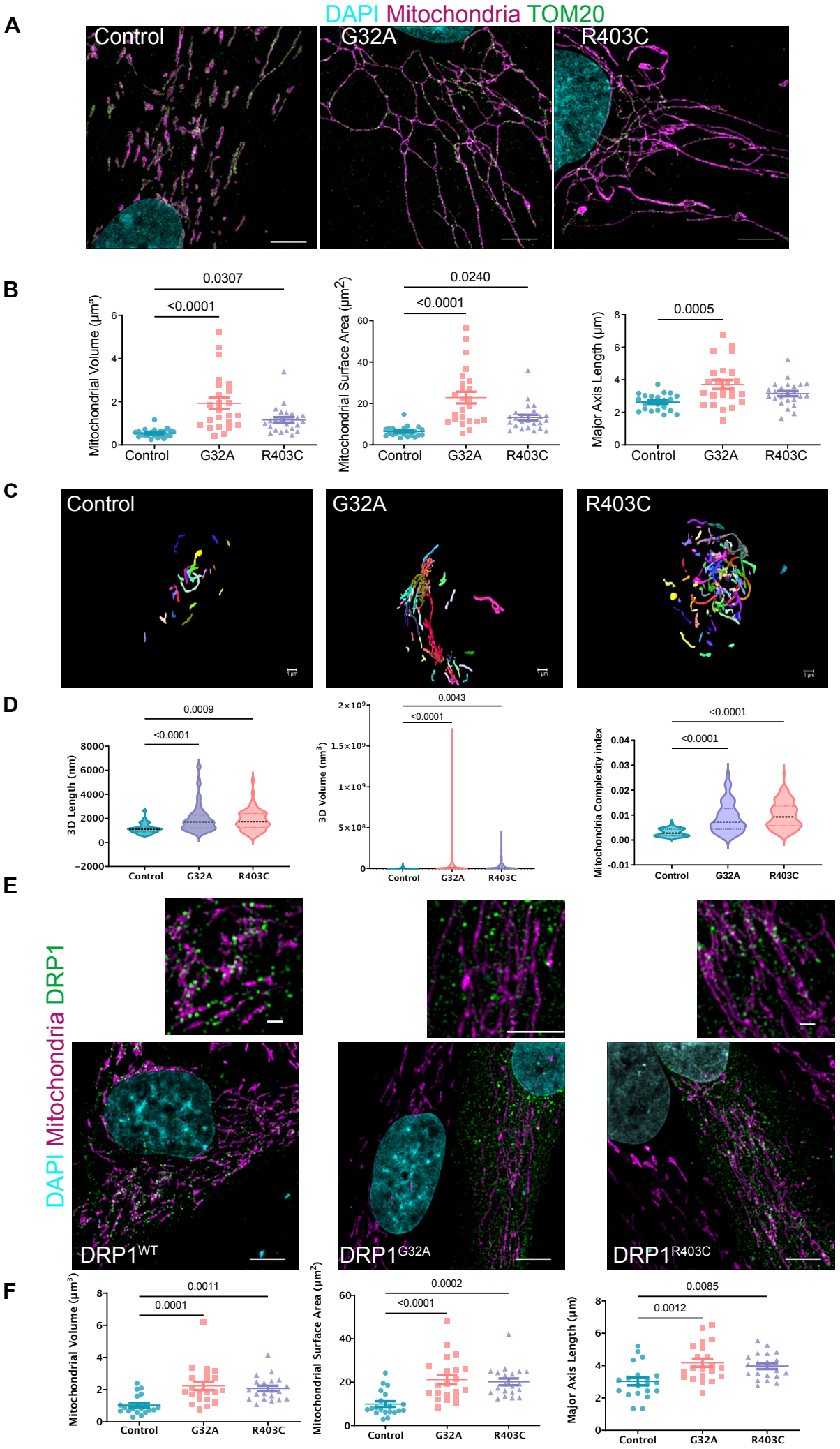
A
DAPI Mitochondria TOM20
Control
G32A
R403C
B
0.0307
<0.0001
Mitochondrial Volume (µm³)
Control
G32A
R403C
0.0240
<0.0001
Mitochondrial Surface Area (µm²)
0.0005
Major Axis Length (µm)
C
Control
G32A
R403C
D
0.0009
<0.0001
3D Length (nm)
0.0043
<0.0001
3D Volume (nm³)
<0.0001
<0.0001
Mitochondria Complexity index
E
DAPI Mitochondria DRP1
DRP1WT
DRP1G32A
DRP1R403C
F
0.0011
0.0001
Mitochondrial Volume (µm³)
0.0002
<0.0001
Mitochondrial Surface Area (µm²)
0.0085
0.0012
Major Axis Length (µm)

Figure 2

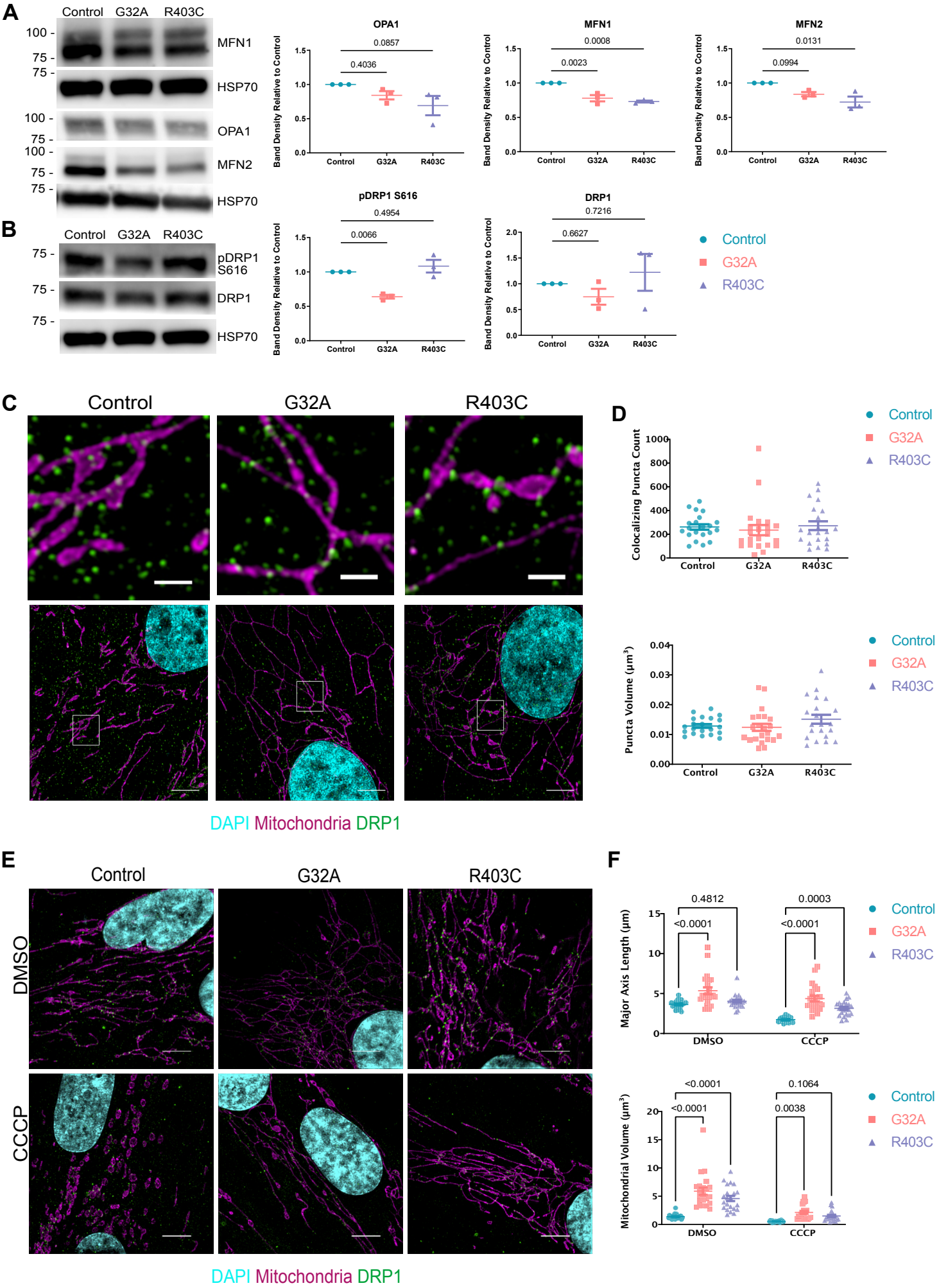
A
Control
G32A
R403C
100 -
75 -
MFN1
HSP70
OPA1
MFN2
Band Density Relative to Control
OPA1
0.0857
0.4036
MFN1
0.0008
0.0023
MFN2
0.0131
0.0994
B
pDRP1 S616
DRP1
pDRP1 S616
0.4954
0.0066
DRP1
0.7216
0.6627
Control
G32A
R403C
C
Control
G32A
R403C
DAPI Mitochondria DRP1
D
Colocalizing Puncta Count
Puncta Volume (μm³)
E
DMSO
CCCP
DAPI Mitochondria DRP1
F
Major Axis Length (μm)
0.4812
<0.0001
0.0003
<0.0001
Mitochondrial Volume (μm³)
<0.0001
<0.0001
0.1064
0.0038

Figure 3

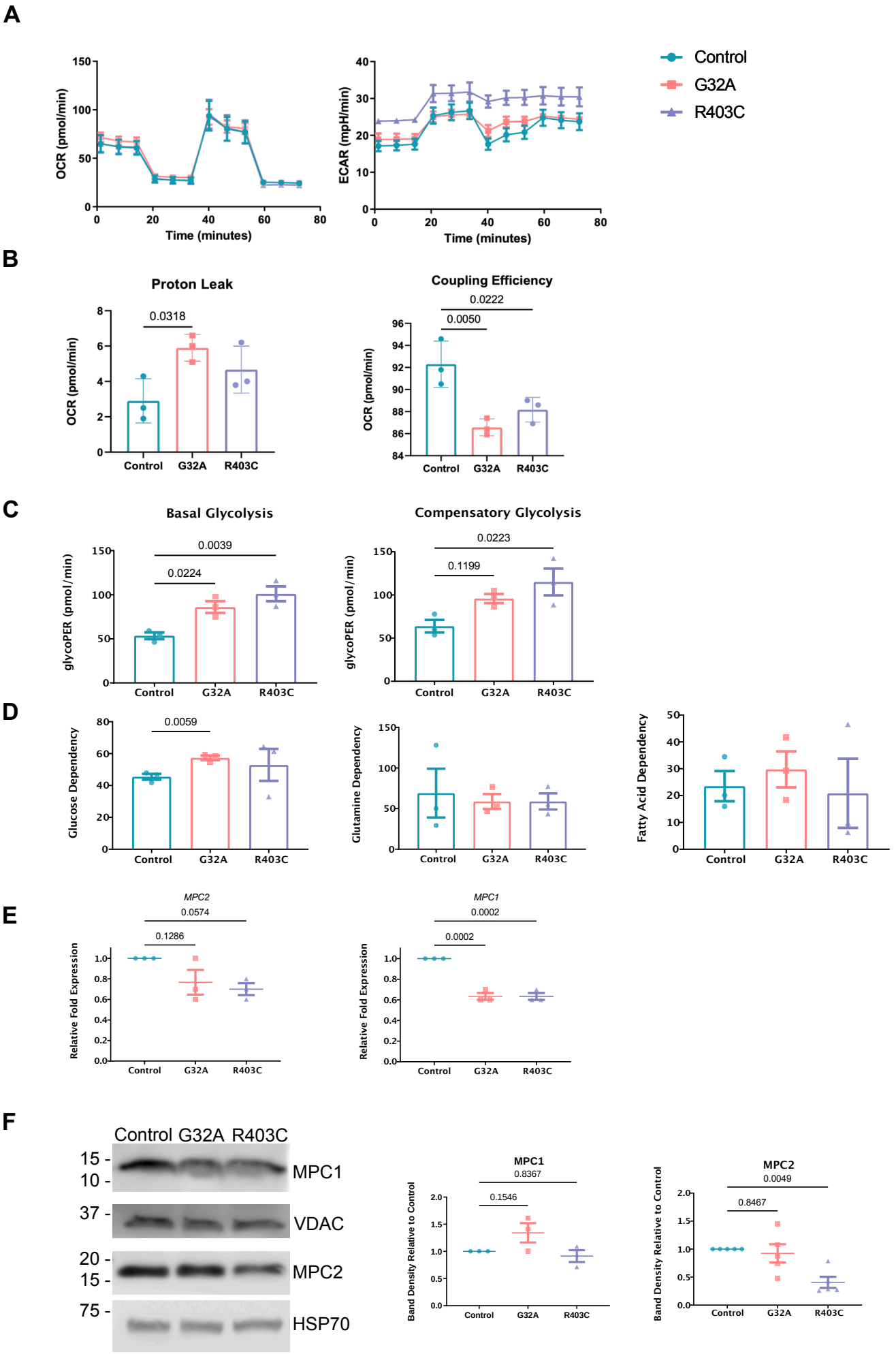
A
OCR (pmol/min)
Time (minutes)
ECAR (mpH/min)
Time (minutes)
Control
G32A
R403C
B
Proton Leak
OCR (pmol/min)
0.0318
Control
G32A
R403C
Coupling Efficiency
OCR (pmol/min)
0.0222
0.0050
Control
G32A
R403C
C
Basal Glycolysis
glycoPER (pmol/min)
0.0039
0.0224
Control
G32A
R403C
Compensatory Glycolysis
glycoPER (pmol/min)
0.0223
0.1199
Control
G32A
R403C
D
Glucose Dependency
0.0059
Control
G32A
R403C
Glutamine Dependency
Control
G32A
R403C
Fatty Acid Dependency
Control
G32A
R403C
E
MPC2
0.0574
0.1286
Relative Fold Expression
Control
G32A
R403C
MPC1
0.0002
0.0002
Relative Fold Expression
Control
G32A
R403C
F
Control G32A R403C
15 -
10 -
MPC1
37 -
VDAC
20 -
15 -
MPC2
75 -
HSP70
MPC1
0.8367
0.1546
Band Density Relative to Control
Control
G32A
R403C
MPC2
0.0049
0.8467
Band Density Relative to Control
Control
G32A
R403C

Figure 4

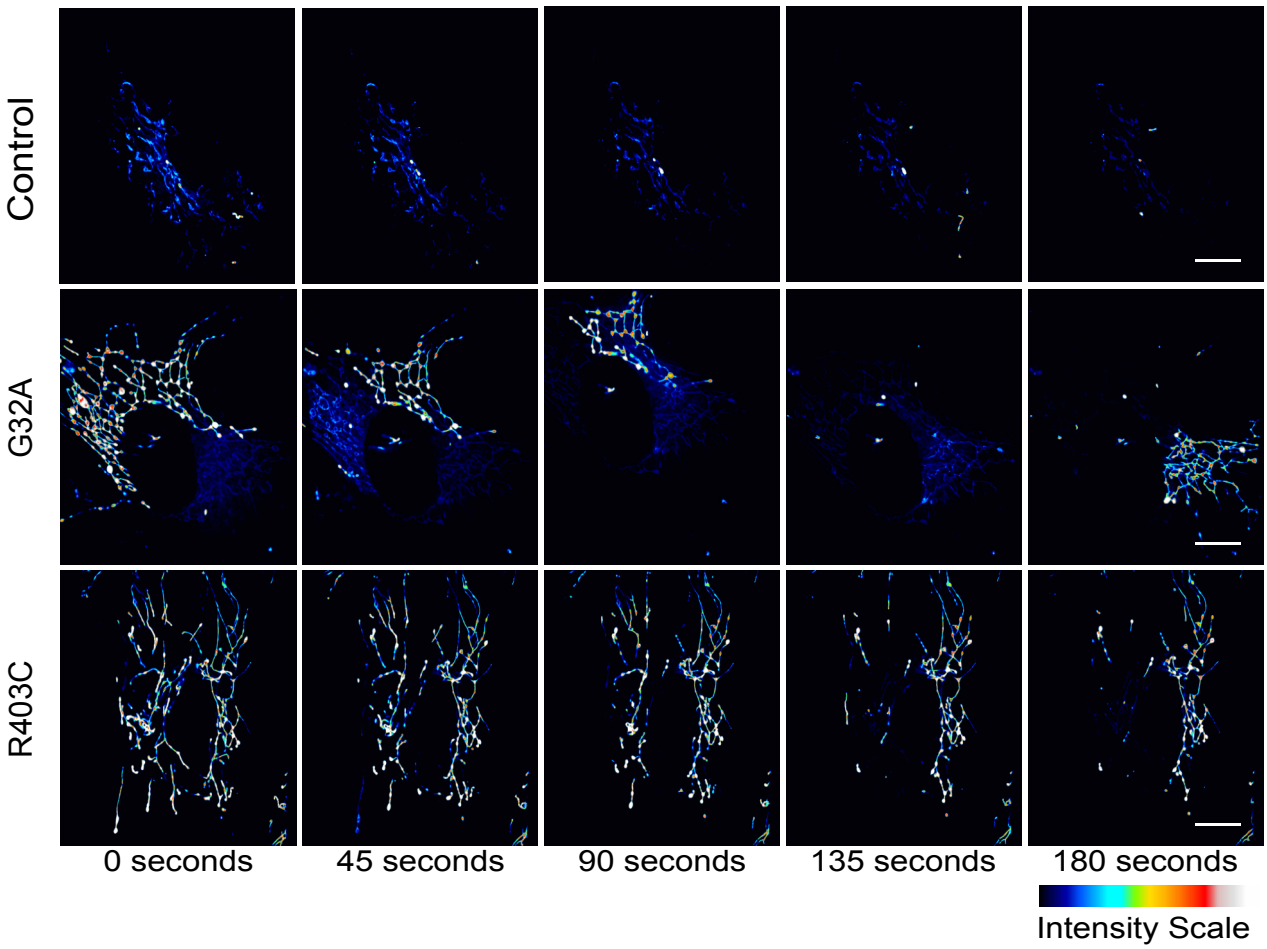
Control
G32A
R403C
0 seconds
45 seconds
90 seconds
135 seconds
180 seconds
Intensity Scale

Figure 5

A

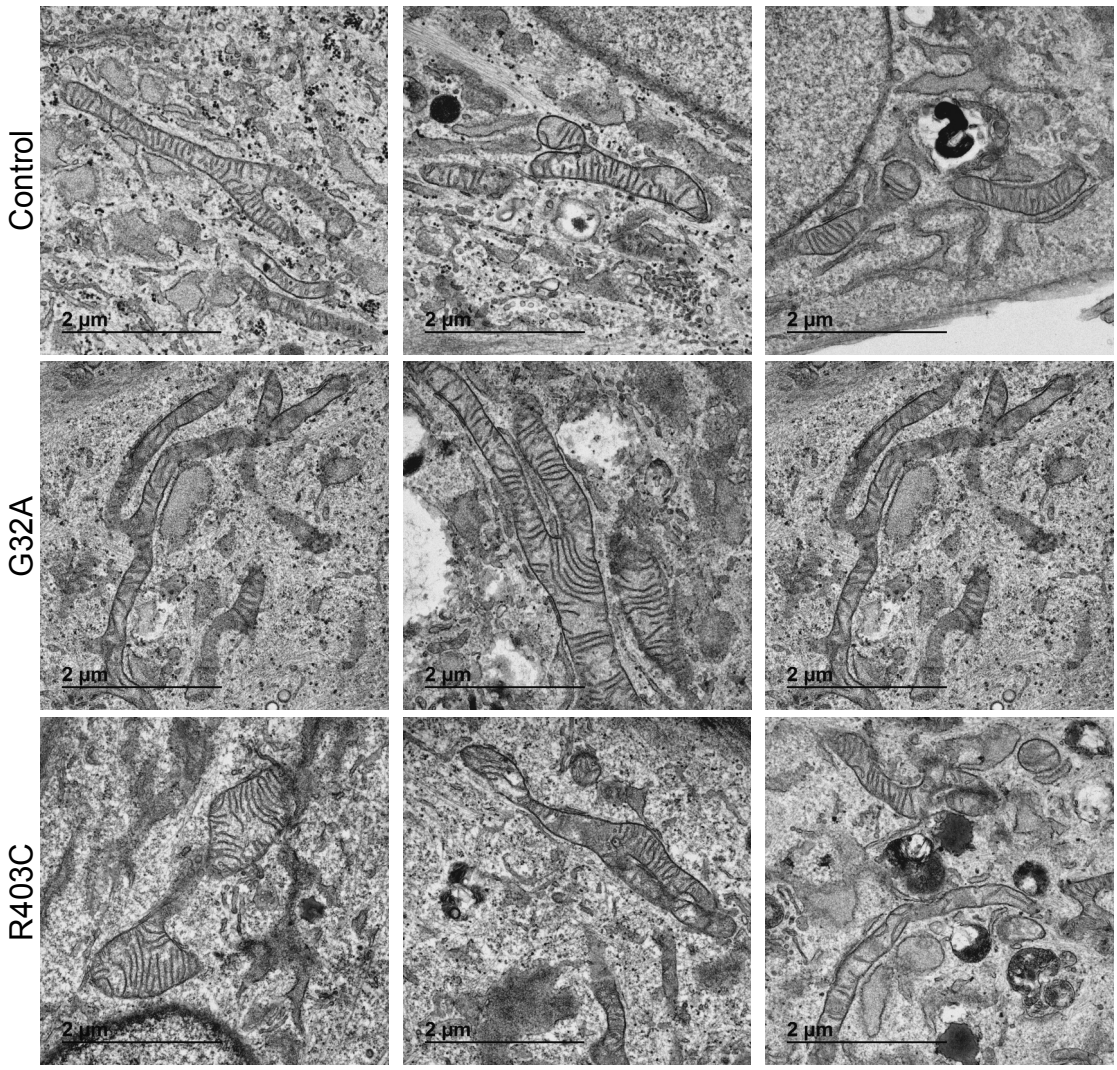
Control
G32A
R403C
2 µm

B

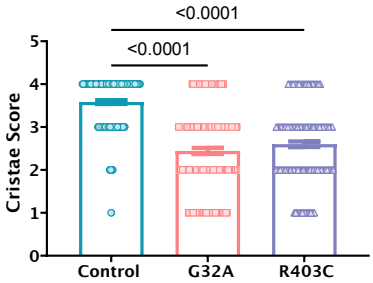
<0.0001
<0.0001
Cristae Score
0
1
2
3
4
5
Control
G32A
R403C

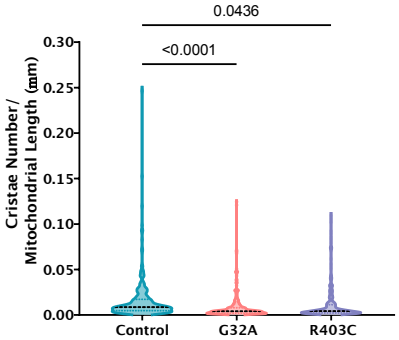
0.0436
<0.0001
Cristae Number/
Mitochondrial Length (µm)
0.00
0.05
0.10
0.15
0.20
0.25
0.30
Control
G32A
R403C

Figure 6

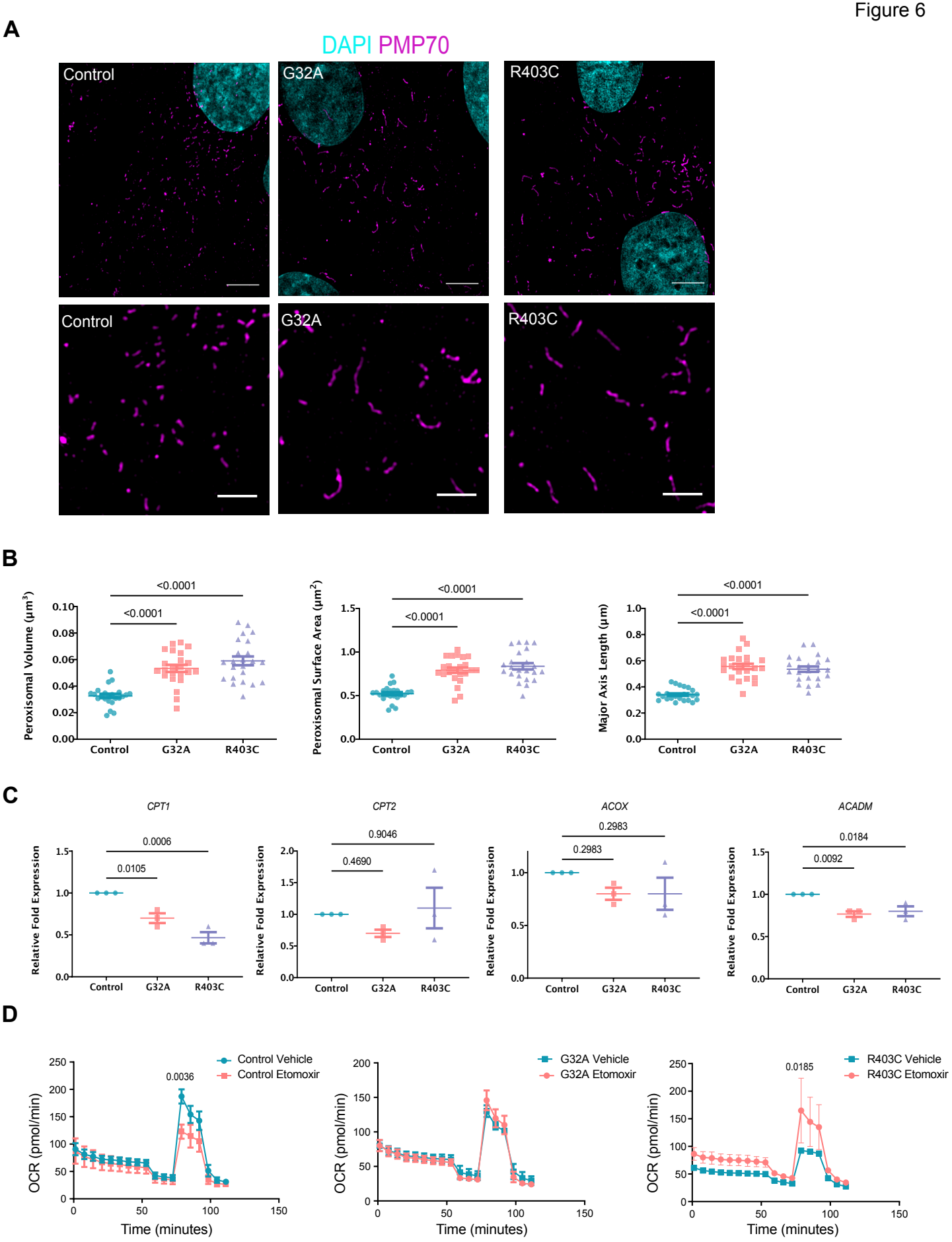
A
DAPI PMP70
Control
G32A
R403C
Control
G32A
R403C
B
Peroxisomal Volume (µm³)
<0.0001
<0.0001
Control
G32A
R403C
Peroxisomal Surface Area (µm²)
<0.0001
<0.0001
Control
G32A
R403C
Major Axis Length (µm)
<0.0001
<0.0001
Control
G32A
R403C
C
CPT1
Relative Fold Expression
0.0006
0.0105
Control
G32A
R403C
CPT2
Relative Fold Expression
0.9046
0.4690
Control
G32A
R403C
ACOX
Relative Fold Expression
0.2983
0.2983
Control
G32A
R403C
ACADM
Relative Fold Expression
0.0184
0.0092
Control
G32A
R403C
D
Control Vehicle
Control Etomoxir
0.0036
OCR (pmol/min)
Time (minutes)
G32A Vehicle
G32A Etomoxir
OCR (pmol/min)
Time (minutes)
R403C Vehicle
R403C Etomoxir
0.0185
OCR (pmol/min)
Time (minutes)

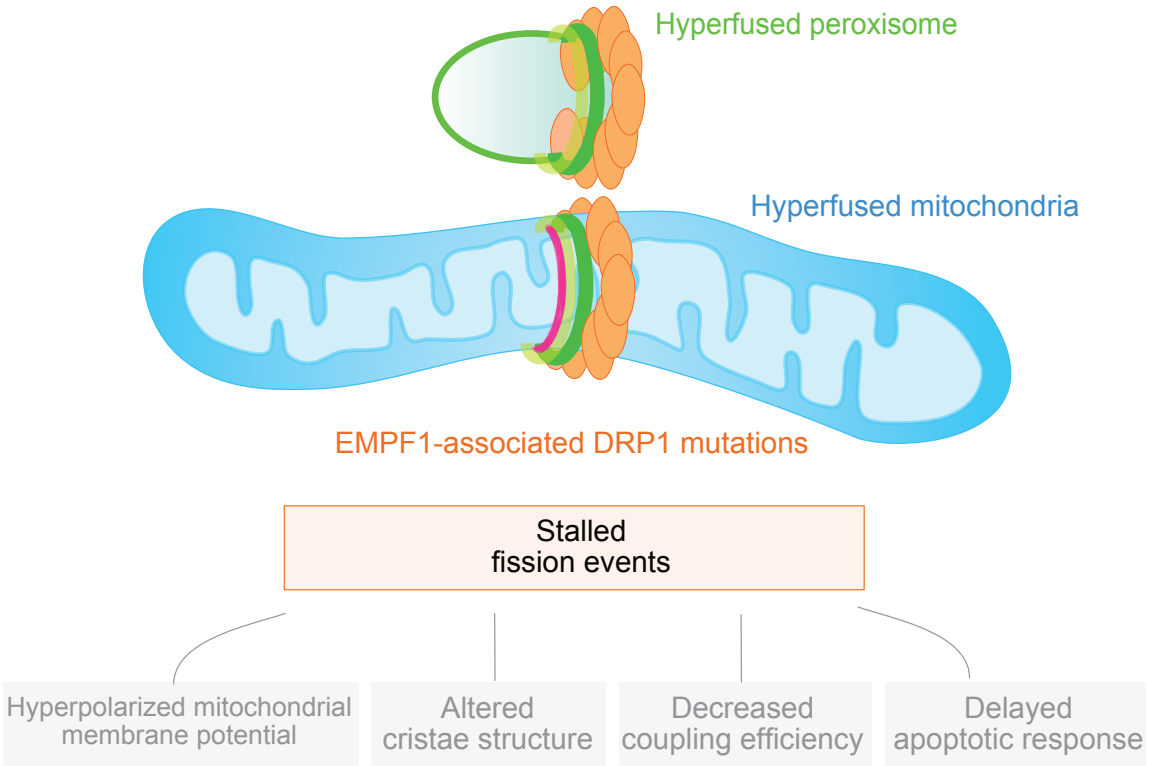
Hyperfused peroxisome
Hyperfused mitochondria
EMPF1-associated DRP1 mutations
Stalled
fission events
Hyperpolarized mitochondrial
membrane potential
Altered
cristae structure
Decreased
coupling efficiency
Delayed
apoptotic response